2023-12

A two-dimensional double layer-averaged model of hyperconcentrated turbidity currents with non-Newtonian rheology

Sun, Y

10.1016/j.ijsrc.2023.08.002
International Journal of Sediment Research
Elsevier BV

A 2D double layer-averaged model of hyperconcentrated turbidity currents with non-Newtonian rheology

Yining Sun[1], Ji Li[1,2], Zhixian Cao[1*] and Alistair G.L. Borthwick[3,4]

1 State Key Laboratory of Water Resources and Hydropower Engineering Science, Wuhan University, Wuhan 430072, China

2 Zienkiewicz Centre for Computational Engineering, Faculty of Science and Engineering, Swansea University, Swansea SA1 8EN, UK

3 Institute for Infrastructure and Environment, The University of Edinburgh, Edinburgh EH9 3JL, UK

4 School of Engineering, Computing and Mathematics, University of Plymouth, Plymouth PL4 8AA, UK

Correspondence

* Zhixian Cao, State Key Laboratory of Water Resources and Hydropower Engineering Science, Wuhan University, Wuhan 430072, China. E-mail: zxcao@whu.edu.cn

ABSTRACT

Hyperconcentrated turbidity currents typically display non-Newtonian characteristics that influence active sediment transport and morphological evolution in alluvial rivers. However, hydro-sediment-morphological processes involving hyperconcentrated turbidity currents are poorly understood to date, with little known about the effect of non-Newtonian rheology. This paper extends a recent 2D double layer-averaged model to incorporate non-Newtonian constitutive relations. The extended model is benchmarked against experimental and numerical data for cases including subaerial mud flow, subaqueous debris flow, and reservoir turbidity currents. The computational results agree well with observations of subaerial mud flow and independent numerical simulations of subaqueous debris flow. Differences between the non-Newtonian and Newtonian model results become more pronounced in terms of propagation distance and sediment transport rate as sediment concentration increases. The model is then applied to turbidity currents in Guxian Reservoir, middle Yellow River, China, which connects to a tributary featuring hyperconcentrated sediment-laden flow. The non-Newtonian model predicts slower propagation of turbidity currents and more significant bed aggradation at the confluence than its Newtonian counterpart. This could be of considerable importance when optimizing reservoir operation schemes.

KEYWORDS

Double layer-averaged model; non-Newtonian rheology; Mud flow; Reservoir turbidity current; Yellow River

1. Introduction

Turbidity currents are subaqueous sediment-laden flows driven by the difference in density between the current and the overlying ambient fluid. Hyperconcentrated turbidity currents carrying fine sediment at concentrations exceeding 200 ~ 300 $\mathrm{kg/m^3}$ typically demonstrate non-Newtonian behavior, especially in the ocean and sandy rivers (Cao and Pender et al., 2006; Wang and Qi et al., 2009). Examples include submarine sediment slumping on continental slopes and subaerial sediment-laden flows plunging into reservoirs. Submarine mud flows with massive momentum may cause severe damage to offshore structures, subsea pipelines, and communication cables, and even trigger tsunamis (Qian and Xu et al., 2020). Reservoir turbidity currents in alluvial rivers may lead to abnormal hydro-sediment-morphological characteristics in reservoirs, such as enhanced sedimentation and, consequently, high flood levels (Wang and Wu et al., 2007). In such cases, a mathematical model capable of resolving hyperconcentrated turbidity currents is essential for river management; prime examples are given by the Yellow River and its tributaries in China, where volumetric sediment concentration can reach 0.3 or beyond during a flood event (Zhang and Xie, 1993).

In practice, it is difficult to measure the hydro-sediment-morphological processes of relatively highly concentrated turbidity currents in the field (Wright and Wiseman et al., 1988). Unlike the numerous laboratory experiments concerning dilute turbidity currents that exhibit Newtonian behavior (Lee and Yu, 1997; Fedele and García, 2009), only a few attempts have been made to study relatively highly concentrated turbidity currents or mud flows exhibiting non-Newtonian behavior (Hallworth and Huppert, 1998; Jacobson and Testik, 2013). Numerical modelling therefore provides a very useful means of studying non-Newtonian, hyperconcentrated turbidity currents. At present, full three-dimensional models incur excessive computational cost and so are not feasible for large-scale, long-duration simulations (Denlinger and Iverson, 2001; Georgoulas and Angelidis et al., 2010; Wang and Chen et al., 2016). Many one-dimensional models have been proposed to investigate hyperconcentrated sediment-laden flows (Brufau and Garcia-Navarro et al., 2000; Imran and Parker et al., 2001; Guo and Hu et al., 2008; Xia and Tian, 2022). Such models neglect interactions between subaqueous flows and ambient fluid, and are inherently unable to simulate lateral spreading. For example, Imran et al. (2001) numerically solved the continuity and momentum equations for mud flow incorporating either Herschel-Bulkley or bilinear rheology, while neglecting the spatialtemporal variation in sediment concentration and the feedback effect from morphological evolution. Two-dimensional (2D) layer-averaged models offer a compromise between computational expense and theoretical accuracy, and so are more suitable for the simulation of hyperconcentrated turbidity currents. Even so, the majority of such models are limited to a single layer or based on an empirical plunge criterion, whereby only the subaqueous sediment-laden flow layer is modelled, and movement of the upper ambient fluid is neglected (Lai and Huang et al., 2015; Hu and Li, 2020; Adebiyi and Hu, 2021), or differences between incipient and stable plunge criteria are ignored (Wang and Xia et al., 2016; Wang and Xia et al., 2018). The foregoing models simply resolve the propagation of turbidity currents after their formation, but are unable to reproduce the impact of reservoir operations on turbidity current formation and propagation. To the authors' knowledge, the coupled 2D double layer-averaged model proposed by Cao et al. (2015) is uniquely capable of resolving the whole processes of dilute reservoir turbidity currents from formation and propagation to recession, as well as bed evolution. However, the model neglects non-Newtonian characteristics of relatively highly concentrated turbidity currents.

In practice, the viscosity of a hyperconcentrated turbidity current alters according to the material strain rate, and so its rheology obeys a non-Newtonian constitutive law, which is quite distinct from that of a dilute flow. Experimental studies have revealed that the rheology of non-Newtonian flows can be approximately expressed using linear (e.g., Bingham), non-linear (O' Brien and Julien, 1988; Huang and Garcia, 1997; Imran and Parker et al., 2001; Balmforth and Provenzale, 2010), or bilinear constitutive laws (Locat, 1997). Among these viscoplastic models, the Herschel-Bulkley model, which incorporates the effects of both shear thinning and yield stress, is most generally suitable for expressing the non-linear characteristics of non-Newtonian flows. Physically, shear thinning and yield stress effects are fundamentally responsible for the rheological differences between Newtonian and non-Newtonian flows. The rheological properties of hyperconcentrated turbidity currents also significantly influence the suspension state of sediment particles, sediment exchange between the flow and the mobile bed, and sediment transport.

Although numerous studies on turbidity currents have examined dilute mixtures exhibiting Newtonian behavior (Lee and Yu, 1997; Fedele and García, 2009; Cao and Li et al., 2015; Hu and Li, 2020), previous layer-averaged models incorporating non-Newtonian rheology have been confined to a single layer (Lai and Huang et al., 2015; Hu and Li, 2020; Adebiyi and Hu, 2021) neglecting the movement of upper layer. In actuality, both non-Newtonian rheology and inter-layer interactions are crucial to the evolution of a hyperconcentrated turbidity current. Herein, we extend the double layer-averaged model proposed by Cao et al. (2015) from dilute to hyperconcentrated currents by incorporating two essential non-Newtonian properties. Our model is benchmarked against a portfolio of experimental and numerical cases, including subaerial mud flow (Wright, 1987; Wright and Krone, 1987), subaqueous debris flow (Imran and Parker et al., 2001), and reservoir turbidity currents (Wang and Wang et al., 2020). We also carry out a field-scale numerical study of a large-scale, long-duration turbidity current in the Guxian Reservoir, Yellow River, to demonstrate the capability of the present extended model. The overall aim of the extended model is to provide insight into the underlying effects of rheology on hydro-sediment-morphological processes related to hyperconcentrated turbidity currents in sandy rivers. Such insight is essential for the optimization of reservoir operation schemes where hyperconcentrated turbidity currents may occur.

2. Mathematical model

2.1. Governing equations

In this section, we develop an extended double layer-averaged (EDL) model by modifying the original double layer-averaged (ODL) model proposed by Cao et al. (2015) to include the rheological effect of a non-Newtonian fluid. The double layer-averaged model comprises: (i) an upper clear-water flow layer; (ii) a lower sediment-laden flow layer (i.e., turbidity current); and (iii) an erodible bed with vanishing velocity (see Fig. S1 in the Supporting Information).

2.1.1. Upper clear-water flow layer

Adopting the mild slope assumption and shallow water approximations, the 2D continuity and momentum equations for the upper clear-water flow layer may be written:

$$\frac{\partial \eta}{\partial t}+\frac{\partial h_w U_w}{\partial x}+\frac{\partial h_w V_w}{\partial y}=-E_w+\frac{\partial \eta_s}{\partial t} \tag{1}$$

$$\frac{\partial h_w U_w}{\partial t}+\frac{\partial}{\partial x}\left[h_w U_w^2+0.5g\left(\eta^2\text{-}2\eta\eta_s\right)\right]+\frac{\partial}{\partial y}\left(h_w U_w V_w\right)=-\frac{\tau_{wx}}{\rho_w}-g\eta\frac{\partial \eta_s}{\partial x}-E_w U_w \tag{2a}$$

$$\frac{\partial h_w V_w}{\partial t}+\frac{\partial}{\partial x}\left(h_w U_w V_w\right)+\frac{\partial}{\partial y}\left[h_w V_w^2+0.5g\left(\eta^2\text{-}2\eta\eta_s\right)\right]=-\frac{\tau_{wy}}{\rho_w}-g\eta\frac{\partial \eta_s}{\partial y}-E_w V_w \tag{2a}$$

where t is time; g is the acceleration due to gravity; x and y are horizontal coordinates; h_w is the thickness of the upper clear-water flow layer; U_w and V_w are clear-water flow layer-averaged velocity components in the *x*- and *y*-directions respectively; η is the elevation of water surface above a fixed horizontal datum; η_s is the elevation of the interface between the clear-water and sediment-laden flow layers above the same datum; ρ_w is the density of water; τ_w is the shear stress at the interface between the two layers; and E_w is water entrainment flux across the interface between the two layers. Equations (1) and (2) facilitate interactions between the ambient water and subaqueous sediment-laden flow, including water exchange E_w from the upper layer to the lower layer and interfacial resistance τ_w between the two layers.

2.1.2. Lower sediment-laden flow layer – turbidity currents

For ease of description, the 2D continuity and momentum equations for the lower sediment-laden flow layer (i.e., turbidity current) and the mass conservation equation for sediment carried by the flow are written in a format similar to that of Cao et al. (2015) as follows (see Supporting Information for the detailed derivation):

$$\frac{\partial \eta_s}{\partial t}+\frac{\partial h_s U_s}{\partial x}+\frac{\partial h_s V_s}{\partial y}=E_w \tag{3}$$

$$\begin{aligned}&\frac{\partial h_s U_s}{\partial t}+\frac{\partial}{\partial x}\left[h_s U_s^2+0.5g\left(\eta_s^2-2\eta_s z_b\right)\right]+\frac{\partial}{\partial y}\left(h_s U_s V_s\right)=-g\eta_s\frac{\partial z_b}{\partial x}-\frac{\rho_w g}{\rho_c}h_s\frac{\partial h_w}{\partial x}\\&-\frac{\left(\rho_0-\rho_c\right)\left(E-D\right)U_s}{\left(1-p\right)\rho_c}+\frac{\left(\rho_s-\rho_w\right)c_s U_s E_w}{\rho_c}+\frac{\rho_w E_w U_w}{\rho_c}-\frac{\left(\rho_s-\rho_w\right)g h_s^2}{2\rho_c}\frac{\partial c_s}{\partial x}+\frac{\tau_{wx}+\tau_{effx}}{\rho_c}\end{aligned} \tag{4a}$$

$$\begin{aligned}&\frac{\partial h_s V_s}{\partial t}+\frac{\partial}{\partial x}\left(h_s U_s V_s\right)+\frac{\partial}{\partial y}\left[h_s V_s^2+0.5g\left(\eta_s^2-2\eta_s z_b\right)\right]=-g\eta_s\frac{\partial z_b}{\partial y}-\frac{\rho_w g}{\rho_c}h_s\frac{\partial h_w}{\partial y}\\&-\frac{\left(\rho_0-\rho_c\right)\left(E-D\right)V_s}{\left(1-p\right)\rho_c}+\frac{\left(\rho_s-\rho_w\right)c_s V_s E_w}{\rho_c}+\frac{\rho_w E_w V_w}{\rho_c}-\frac{\left(\rho_s-\rho_w\right)g h_s^2}{2\rho_c}\frac{\partial c_s}{\partial y}+\frac{\tau_{wy}+\tau_{effy}}{\rho_c}\end{aligned} \tag{4b}$$

$$\frac{\partial h_s c_s}{\partial t}+\frac{\partial h_s U_s c_s}{\partial x}+\frac{\partial h_s V_s c_s}{\partial y}=E-D \tag{5}$$

where h_s is the thickness of the lower sediment-laden flow layer; U_s and V_s are the sediment-laden flow layer-averaged velocity components in the x- and y-directions respectively; c_s is volumetric sediment concentration; z_b is bed elevation; p is bed sediment porosity; ρ_s is sediment density; $\rho_c = \rho_w(1-c_s) + \rho_s c_s$ is the density of the water-sediment mixture in the turbidity current layer; $\rho_0 = \rho_w p + \rho_s(1-p)$ is the density of the saturated bed; τ_w is the shear stress at the interface between the clear-water and sediment-laden flow layers; and E, D are the sediment entrainment flux and sediment deposition flux respectively.

We define the effective shear stress as $\tau_{eff} = -\left(\beta_B \tau_B + \beta_N \tau_N\right)$ where τ_B is the shear stress due to non-Newtonian rheology and τ_N is the shear stress due to Newtonian rheology. In practice, hyperconcentrated flows may be progressively diluted until eventually transforming into Newtonian fluid in cases where the current is sufficiently dilute (Pierson and Scott, 1985); hence, the coefficients β_B and β_N are introduced to control the Newtonian or non-Newtonian behavior according to sediment concentration. Experimental studies have collectively shown that $\beta_B = 0$ and $\beta_N = 1$ for a 'Newtonian' water-sediment mixture with low sediment concentration (less than about 200 ~ 300 $\mathrm{kg/m^3}$). When the sediment concentration is high, the lower sediment-laden flow layer acts as a non-Newtonian fluid, such that $\beta_B = 1$ and $\beta_N = 0$.

Of the many formulations proposed for non-Newtonian rheology, the most common approximations for τ_B are given by Bingham, Herschel-Bulkley, and bilinear constitutive models (Locat, 1997). Herein, we select the Herschel-Bulkley model which explicitly incorporates primary non-Newtonian effects, i.e., shear-thinning and yield-stress:

$$\begin{cases} \tau_B = \left(\tau_Y + \mu_Y |\gamma|^n\right)\mathrm{sgn}(\gamma) & |\tau_B| > \tau_Y \\ \gamma = 0 & |\tau_B| \le \tau_Y \end{cases} \tag{6}$$

where τ_Y is yield stress; $\gamma = \dfrac{\partial u}{\partial z}$ is shear rate; $\tau_V = \mu_Y (\gamma)^n$ is viscous stress; and μ_Y is the fluid consistency; and the power index $n = 1$ denotes a linear Bingham model, $n < 1$ denotes shear-thinning, and $n > 1$ is shear-thickening.

The momentum conservation equations incorporating the Herschel-Bulkley model for sediment-laden flow layer are:

$$\begin{aligned} \frac{\partial h_s U_s}{\partial t} + \frac{\partial}{\partial x}\left[h_s U_s^2 + 0.5g\left(\eta_s^2 - 2\eta_s z_b\right)\right] + \frac{\partial}{\partial y}\left(h_s U_s V_s\right) = -g\eta_s \frac{\partial z_b}{\partial x} - \frac{\rho_w g}{\rho_c} h_s \frac{\partial h_w}{\partial x} \\ - \frac{(\rho_0 - \rho_c)(E - D)U_s}{(1-p)\rho_c} + \frac{(\rho_s - \rho_w)c_s U_s E_w}{\rho_c} + \frac{\rho_w E_w U_w}{\rho_c} - \frac{(\rho_s - \rho_w) g h_s^2}{2\rho_c}\frac{\partial c_s}{\partial x} \\ + \frac{\tau_{wx}}{\rho_c} - \beta_N \frac{\tau_{Nx}}{\rho_c} - \frac{\beta_B}{\rho_c}\left[\left(\frac{\tau_{Yx}}{|\gamma_x|} + \mu_Y |\gamma_x|^{n-1}\right)\gamma_x\right]\Bigg|_{z=z_b} \end{aligned} \tag{7a}$$

$$\begin{aligned} \frac{\partial h_s V_s}{\partial t} + \frac{\partial}{\partial x}\left(h_s U_s V_s\right) + \frac{\partial}{\partial y}\left[h_s V_s^2 + 0.5g\left(\eta_s^2 - 2\eta_s z_b\right)\right] = -g\eta_s \frac{\partial z_b}{\partial y} - \frac{\rho_w g}{\rho_c} h_s \frac{\partial h_w}{\partial y} \\ - \frac{(\rho_0 - \rho_c)(E - D)V_s}{(1-p)\rho_c} + \frac{(\rho_s - \rho_w)c_s V_s E_w}{\rho_c} + \frac{\rho_w E_w V_w}{\rho_c} - \frac{(\rho_s - \rho_w) g h_s^2}{2\rho_c}\frac{\partial c_s}{\partial y} \\ + \frac{\tau_{wy}}{\rho_c} - \beta_N \frac{\tau_{Ny}}{\rho_c} - \frac{\beta_B}{\rho_c}\left[\left(\frac{\tau_{Yy}}{|\gamma_y|} + \mu_Y |\gamma_y|^{n-1}\right)\gamma_y\right]\Bigg|_{z=z_b} \end{aligned} \tag{7b}$$

A detailed derivation of the governing equations obtained using the bilinear constitutive law is given in the Supporting Information.

2.1.3. Erodible bed

The mass conservation equation for bed sediment is

$$\frac{\partial z_b}{\partial t} = -\frac{E-D}{1-p} \tag{8}$$

where z_b is the bed elevation above the fixed horizontal datum; p is the bed sediment porosity; E is the sediment entrainment flux; and D is the sediment deposition flux.

2.2. Model closure

To close the governing equations, a set of relationships is introduced to determine the water entrainment E_w, sediment exchange flux (i.e., entrainment E minus deposition D), interface shear stress, and bed boundary resistance, as per Cao et al. (2015). Following Parker et al. (1986), the water entrainment mass flux E_w is calculated from

$$E_w = e_w \overline{U}_{ws} \tag{9}$$

where $\overline{U}_{ws} = \sqrt{(U_w - U_s)^2 + (V_w - V_s)^2}$ is the magnitude of the resultant velocity difference between the two layers; and the water entrainment coefficient e_w is estimated from

$$e_w = \frac{0.00153}{0.0204 + \mathrm{Ri}} \tag{10}$$

in which the Richardson number $\mathrm{Ri} = sgc_s h_s / \overline{U}_{ws}^2$ and the specific gravity of sediment $s = (\rho_s / \rho_w)\text{-}1$. The following formulae are used to calculate the sediment entrainment and deposition flux,

$$D = \omega c_s \left(1 - c_s\right)^m \tag{11}$$

$$E = \omega E_{\mathrm{s}} \tag{12}$$

Hindered sediment settling velocity is taken into account in Eq. (11), using the relationship determined by Richardson and Zaki (1997). The power m is estimated from $m = 4.45 R_p^{-0.1}$, in which $R_p = \omega d/\nu$ is the particle Reynolds number, where ω is the settling velocity of a single sediment particle in tranquil clear water, calculated using the formula of Zhang and Xie (1993) as

$$\omega = \sqrt{(13.95\frac{\nu}{d})^2 + 1.09sgd} - 13.95\frac{\nu}{d} \tag{13}$$

where d is the sediment particle diameter and ν is the kinematic viscosity of water. In evaluating Eq. (12), we use the following empirical formula proposed by Zhang and Xie (1993), which is well-tested and widely used for suspended sediment transport in the open channel flow of the Yellow River, China:

$$E_s = \frac{1}{20\rho_s}\frac{(\overline{U}_s^3 / gh_s\omega)^{1.5}}{1+(\overline{U}_s^3 / 45gh_s\omega)^{1.15}} \tag{14}$$

Manning's formula is used to calculate resistance relationships between the upper layer clear water flow, the lower layer sediment-laden flow, and the erodible bed as follows (Cao et al., 2015):

$$\tau_{wx} = \rho_w g n_i^2 (U_w - U_s)\overline{U}_{ws} / h_w^{1/3} \tag{15a}$$

$$\tau_{wy} = \rho_w g n_i^2 (V_w - V_s)\overline{U}_{ws} / h_w^{1/3} \tag{15b}$$

$$\tau_{Nx} = \rho_c g n_b^2 U_s \overline{U}_s / h_s^{1/3} \tag{16a}$$

$$\tau_{Ny} = \rho_c g n_b^2 V_s \overline{U}_s / h_s^{1/3} \tag{16b}$$

where n_i is the Manning coefficient representing friction at the interface between the sediment-laden flow layer and clear-water flow layer; n_b is the Manning coefficient representing bed roughness; and $\overline{U}_s = \sqrt{U_s^{\,2} + V_s^{\,2}}$ is the resultant velocity of the sediment-laden flow layer.

The equation derivations involve a rheological model that represents non-Newtonian fluid characteristics though the effective bed shear stress τ_{eff}. One of the pivotal issues in non-Newtonian fluid simulation is the estimation of the yield stress τ_Y and viscous stress $\tau_V \left(= \mu_Y \gamma^n\right)$ which are determined either by calibration against measured data or by using empirical relations, such as the formulae proposed by Fei et al. (1991):

$$\tau_Y = 0.098 \exp\left(8.45 \frac{c_s - c_{v0}}{c_{vm}} + 1.5\right) \tag{17}$$

$$\mu_Y = \mu_0 \left(1 - k\, c/c_{vm}\right)^{-2.5} \tag{18}$$

where the sediment limiting concentration $c_{vm} = \phi\left(0.92 + 0.02 \log\left(1/d\right)\right)$, with a correction coefficient ϕ to account for the limited number of sediment samples used in devising the original relation; the threshold concentration of Bingham fluid $c_{vo} = 1.26 c_{vm}^{\;3.2}$; the coefficient $k = 1 + 2.0\left(c_s/c_{vm}\right)^{0.3}\left(1 - c_s/c_{vm}\right)^4$; and μ_0 is the dynamic viscosity of water.

Based on an assumption of non-linear velocity distribution through the depth (Johnson and Kokelaar et al., 2012),

$$u_{si} = (2 - \alpha_n)\left(1 - \left(1 - \frac{z - z_b}{h_s}\right)^{\frac{1}{1-\alpha_n}}\right) U_{si} \tag{19}$$

The velocity gradient components of sediment-laden flow at the basal surface are approximated by

$$\left.\frac{\partial u_s}{\partial z}\right|_{z=z_b} = \frac{2-\alpha_n}{1-\alpha_n}\frac{U_s}{h_s}, \quad \alpha_n = \left[0,1\right) \tag{20a}$$

$$\left.\frac{\partial v_s}{\partial z}\right|_{z=z_b} = \frac{2-\alpha_n}{1-\alpha_n}\frac{V_s}{h_s}, \quad \alpha_n = \left[0,1\right) \tag{20b}$$

where α_n is a profile shape parameter ranging between 0 and 1.

2.3. Numerical algorithm

The governing equations for the lower sediment-laden flow layer are cast as a nonhomogeneous hyperbolic system, with bed shear stress for non-Newtonian rheology expressed as a source term, thus preserving hyperbolicity (Li and Cao et al., 2015). The two hyperbolic systems of governing equations for the two layers are solved separately and synchronously. Each hyperbolic system is solved by a quasi-well balanced numerical algorithm involving drying and wetting, using a second-order accurate finite volume Godunov-type approach in conjunction with the Harten-Lax-van Leer contact wave (HLLC) approximate Riemann solver (Toro, 2001) on a fixed rectangular mesh. Assuming that bed deformation is entirely determined by local entrainment and deposition fluxes in accordance with the non-capacity model of sediment transport, Eq. (8) is solved separately from the remaining equations. A detailed description of the numerical algorithm is given by Cao et al. (2015).

3. Benchmark tests

Here, a series of experimental and numerical benchmark tests is used to validate the present EDL model for subaerial mud flow (Wright, 1987; Wright and Krone, 1987) (see Text S2 in the Supporting Information), subaqueous debris flow, and a reservoir turbidity current. In all cases, fixed uniform meshes are adopted, and refined to ensure mesh independence. The Courant number is set to 0.4, bed porosity $p = 0.4$, and coefficient $\alpha_n = 0$. To quantify discrepancies between computational results and experimental data, the coefficient of determination (R^2) is calculated from:

$$\mathrm{R}^2 = \frac{\left(\sum_{i=1}^{n}\left(E_i^{\mathrm{obs}} - \bar{E}^{\mathrm{obs}}\right)\left(E_i^{\mathrm{com}} - \bar{E}^{\mathrm{com}}\right)\right)^2}{\sum_{i=1}^{n}\left(E_i^{\mathrm{obs}} - \bar{E}^{\mathrm{obs}}\right)^2 \sum_{i=1}^{n}\left(E_i^{\mathrm{com}} - \bar{E}^{\mathrm{com}}\right)^2} \tag{21}$$

where E_i^{obs} represents observed data and $\bar{E}^{\mathrm{obs}}$ is their mean value; E_i^{com} represents computed data and $\bar{E}^{\mathrm{com}}$ is their mean value. The closer R^2 is to 1, the smaller the discrepancy.

3.1. Subaqueous debris flow

A numerical case originally conducted by Imran et al. (2001) is first used to probe into the choice of rheological model on the evolution of subaqueous debris flow. The flow domain comprises a 7200 m long rectangular flume, whose bottom slope is 0.05. The following parameters are specified according to Run AQ of Imran et al. (2001): initial profile of slurry thickness is parabolic of length $L = 600\,\mathrm{m}$ and maximum thickness $h_{s0} = 24\,\mathrm{m}$ at the centre, corresponding to Fig. S4 in the Supporting Information; initial density of debris flow is $\rho_{c0} = 1500\,\mathrm{kg/m^3}$; and debris flow has Bingham rheology (i.e., $n = 1$ in the Herschel-Bulkley model), with yield stress $\tau_Y = 1000\,\mathrm{N/m^2}$ and dynamic viscosity $\mu_Y = 400\,\mathrm{N \cdot s/m^2}$. Grid spacing is 2 m in both longitudinal and lateral directions. Solid boundary conditions for the upper clear-water flow layer and the lower sediment-laden flow layer are implemented through the flux computation approach suggested by Hou et al. (2013).

3.1.1. Model Comparison

Simulations are performed using the present EDL model for the same failure volume, yield stress, and dynamic viscosity as Imran et al.'s model. It should be noted that Imran et al.'s model is applicable only to subaqueous debris flows over a fixed bed and does not account for inter-layer interactions and bed deformation. Hence, water entrainment E_w, interface friction resistance τ_w, and sediment entrainment and deposition fluxes of the present EDL model are all set to zero for the validation test.

Fig. 1 compares the computed thickness of the debris flows by the EDL model (with Bingham rheological relation) with numerical predictions by Imran et al. (2001). The results are presented in non-dimensional form, based on the following horizontal and vertical scales, $L = 600\,\mathrm{m}$ and $h_{s0} = 24\,\mathrm{m}$. In the original numerical case, the initial ambient water depth is difficult to discern, and its effect on debris flow is negligible (see

Fig. S5 in Supporting Information); herein, the initial ambient water depth is set to $50\,h_{s0}$. Fig. 1 shows that the subaqueous debris flows computed using the Imran et al. and EDL models evolve into almost identical profiles. At $t = 2\,\mathrm{min}$, the thickness of debris flow computed using the present EDL model is larger in the front and smaller in the tail than that calculated with the Imran et al. model, whereas the runout distances are nearly identical (Fig. 1a). At $t = 22\,\mathrm{min}$, the final runout distance computed using the present EDL model is marginally longer than that determined by the Imran et al. model (Fig. 1b). From Fig. 1, the computed evolution of debris flow by both models shows reasonable agreement. Slight differences between the computed profiles mainly arise from the distinct physical mechanisms on which the two models are based. In Imran et al.'s model, the debris flow is vertically separated into two zones (i.e., plug layer and shear layer), which requires a series of tuning parameters to have to be implemented, whereas such treatment is not necessary for the present model.

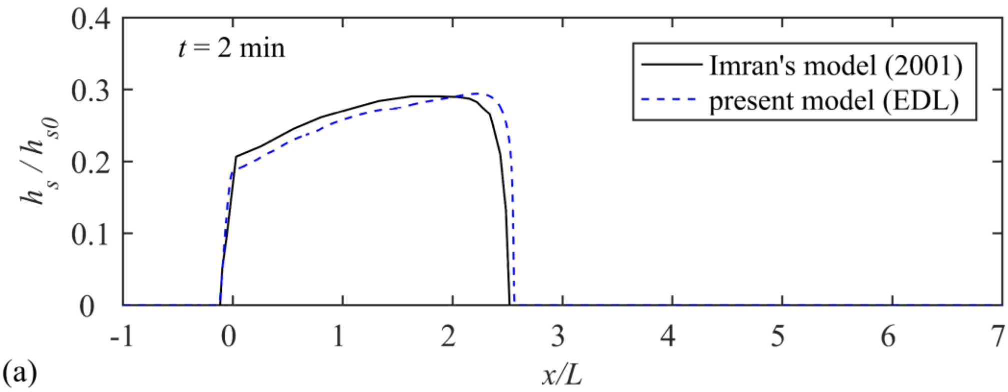

(a)

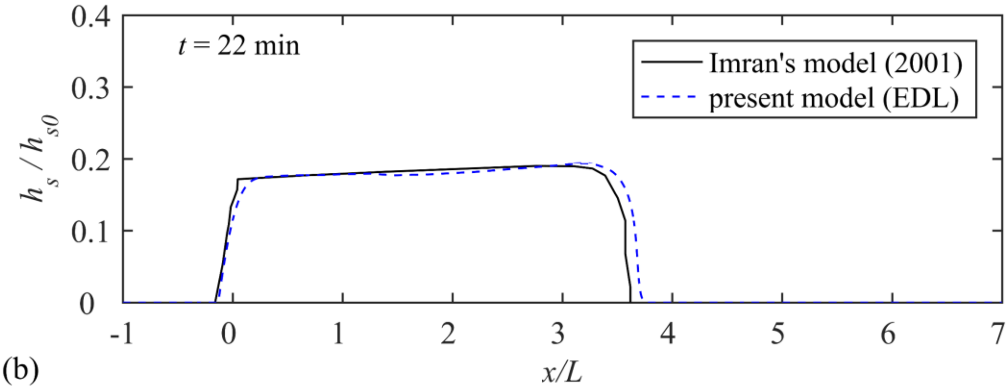

(b)

Fig. 1. Dimensionless thickness of debris flow computed using Imran et al.'s (2001) model and the present EDL model. Water entrainment E_w, interface friction resistance τ_w, and sediment entrainment and deposition fluxes are set to zero in the EDL model.

3.1.2. Sensitivity analysis

We now investigate the sensitivity of the computational predictions by the present EDL model to choice of yield stress τ_Y and power index n. Firstly, n is set to 1 as in the original numerical case, and spatialtemporal variation of the debris flow computed for τ_Y = 0, 500, and $1000\ \mathrm{N/m^2}$. Then, the yield stress τ_Y is set to $1000\ \mathrm{N/m^2}$, the same as in the original numerical case, and n is altered by ± 0.5.

As the yield stress τ_Y decreases from 1000 $\mathrm{N/m^2}$ to zero, the debris flow progressively acts as a Newtonian flow. Fig. 2 superimposes the Bingham flow and Newtonian flow profiles at times t = 2 and 22 min. The following differences between the two flow profiles may be discerned. First, the Bingham flow propagates more slowly than the Newtonian flow. Second, the thickness of the Newtonian flow decreases more rapidly with time than that of the Bingham flow, and its surface has maximum thickness at the front and zero thickness at the tail. Third, the Bingham flow only propagates a finite distance downstream with its front velocity asymptotically falling to zero, whereas the Newtonian flow propagates further downstream. This is primarily because the yield stress of the Bingham flow causes its velocity to decay more rapidly with time than the corresponding Newtonian flow.

The power index n reflects the shear-thinning ($n<1$) or shear-thickening ($n>1$) behavior of a non-Newtonian fluid. Initially, the flow passes through a high shearing rate range, with the power index n representing the extent to which the behaviour is non-linear. Here, the viscous stress is higher for larger n, leading to increased thickness and slower propogation of debris flow (Fig. 2a). The fluid experiences a low shear rate range during the final period, when the runout distance of debris flows varies slightly with n, indicating that the evolution of debris flow due to low shear rate is almost insensitive to choice of n. The debris flow simulated with $n = 0.5$ propagates furthest downstream (Fig. 2b).

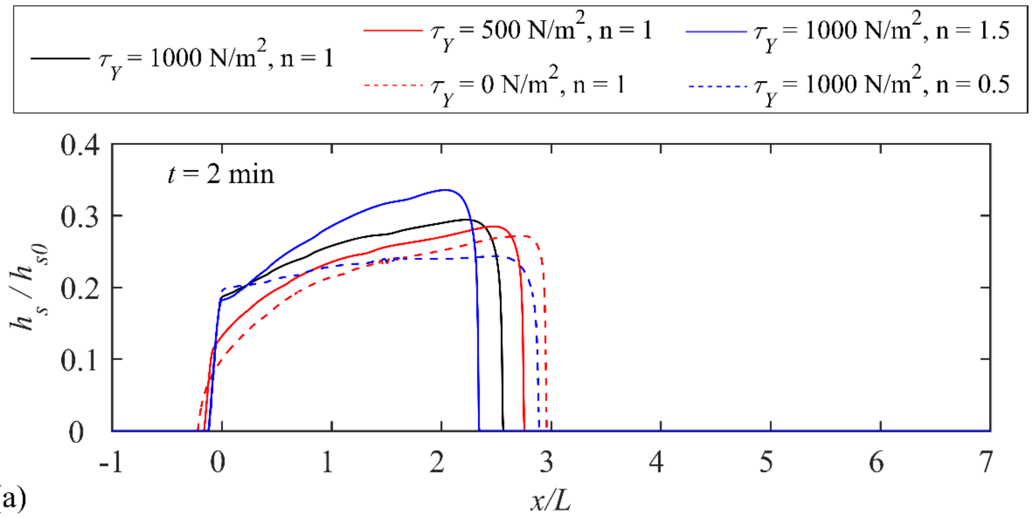

(a)

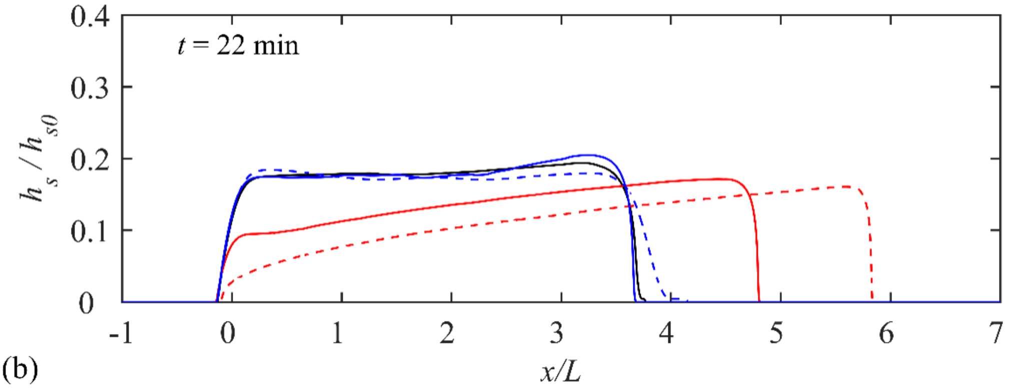

(b)

Fig. 2. Sensitivity of computed dimensionless thickness of debris flow to choice of yield stress τ_Y and power index n at times: (a) $t = 2$ min; and (b) $t = 22$ min. Note that $n = 1$ denotes a linear Bingham model, $n < 1$ represents shear-thinning, and n > 1 denotes shear-thickening.

3.1.3. Effect of interaction between two layers on debris flow evolution

The subaqueous debris flow is stratified vertically, characterized by a double-layer flow structure composed of a subaqueous sediment-laden flow layer immediately above the bed and an upper clear-water flow layer. However, Imran et al.'s (2001) model neglected the effect of inter-layer interactions between the two layers, including water exchange E_w from the upper layer to the lower layer, and interfacial resistance τ_w, both of which are critical for the evolution of a subaqueous debris flow. Fig. 3 displays the effect of interactions between two layers on the evolution of debris flow. It can be seen that the thickness of debris flow decreases as it propagates downstream, owing to current spreading and water entrainment. Initially, the debris flow spreads rapidly, and its thickness decreases with distance. When the effect of water entrainment is included, the interface area between the debris flow and the ambient water increases with time, and so the total amount of water entrained increases. Hence, cases accounting for water entrainment exhibit a larger thickness of debris flow at the front and longer final runout distance than those without. As the Manning roughness coefficient is altered, the debris flow experiences marginally different evolution, indicating that the interfacial resistance τ_w plays a secondary role.

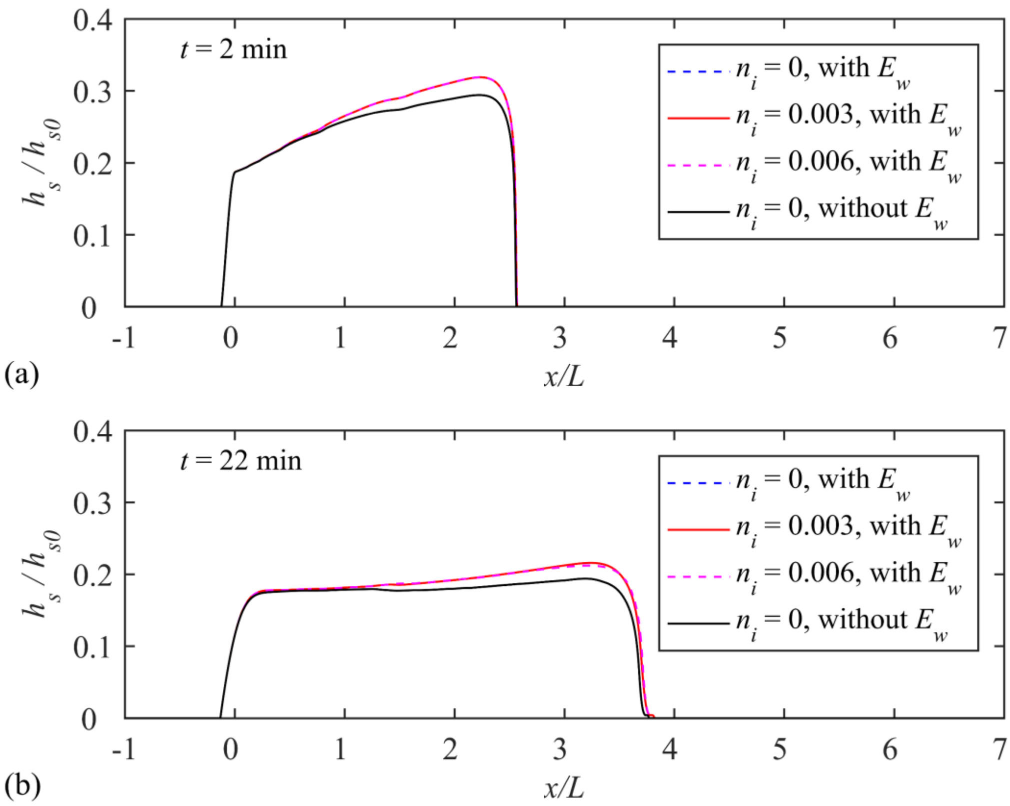

Fig. 3. Debris flow profiles predicted using EDL model for different interface Manning roughness coefficient values n_i = 0, 0.003 and 0.006 m$^{-1/3}$s at times: (a) $t = 2$ min; and (b) $t = 22$ min.

3.1.4. Effect of particle sedimentation on debris flow evolution

Debris flows with high sediment concentration may drive active morphological evolution featuring intensive, complex interactions between flow and bed, which are in turn significant for debris flow evolution. On the one hand, flow stream characteristics, such as density, velocity, and depth, are directly altered by sediment deposition and entrainment. On the other hand, the deformed bed provides morphological feedback to the evolution of the debris flow. However, in Imran et al.'s (2001) model, bed deformation caused by sediment deposition or entrainment is ignored; this omission warrants further discussion.

Figs. 4 and 5 illustrate the evolution of debris flow, bed deformation, and sediment concentration profiles along the channel at two instants, computed for sediment particle diameter values of $d = 9\,\mu\text{m}$, $62.5\,\mu\text{m}$ and 2 mm. Fig. 4 presents the dimensionless bed deformation $\hat{z}_b = (z_b - z_0)/h_{s0}$ and dimensionless interface elevation $\hat{\eta}_s = h_s/h_{s0} + \hat{z}_b$ (where z_0 denotes initial bed elevation) as functions of distance along the channel. At $t = 22\,\text{min}$ (Fig. 4a), much of the sediment settles in the tail of the debris flow obtained for particles of large diameter $d = 2\,\text{mm}$ and the deposition thickness decreases in the direction of the debris flow as it propagates downstream. For finer particles, sedimentation is not apparent. Accordingly, the sediment concentration of the debris flow decreases progressively as the particle diameter increases (Fig. 5). At t = 50 min, the debris flow for $d = 2\,\text{mm}$ slows down. Its sediments are all deposited, corresponding to a state of recession of the debris flow (Fig. 4b). This occurs primarily because bed and interface resistances dissipate the kinetic energy of the debris flow, and water entrained from the ambient fluid dilutes the water-sediment mixture, thus reducing the driving force. By contrast, a debris flow with fine particles produces little sedimentation.

Bed deformation is sensitive to sediment particle diameter, with feedback on the debris flow as it evolves. Specifically, as d increases, the sediment deposition thickness grows, runout distance shortens, and sediment concentration c_s reduces; and so there is a smaller driving force for the debris flow. In short, debris flow with larger d propagates slower.

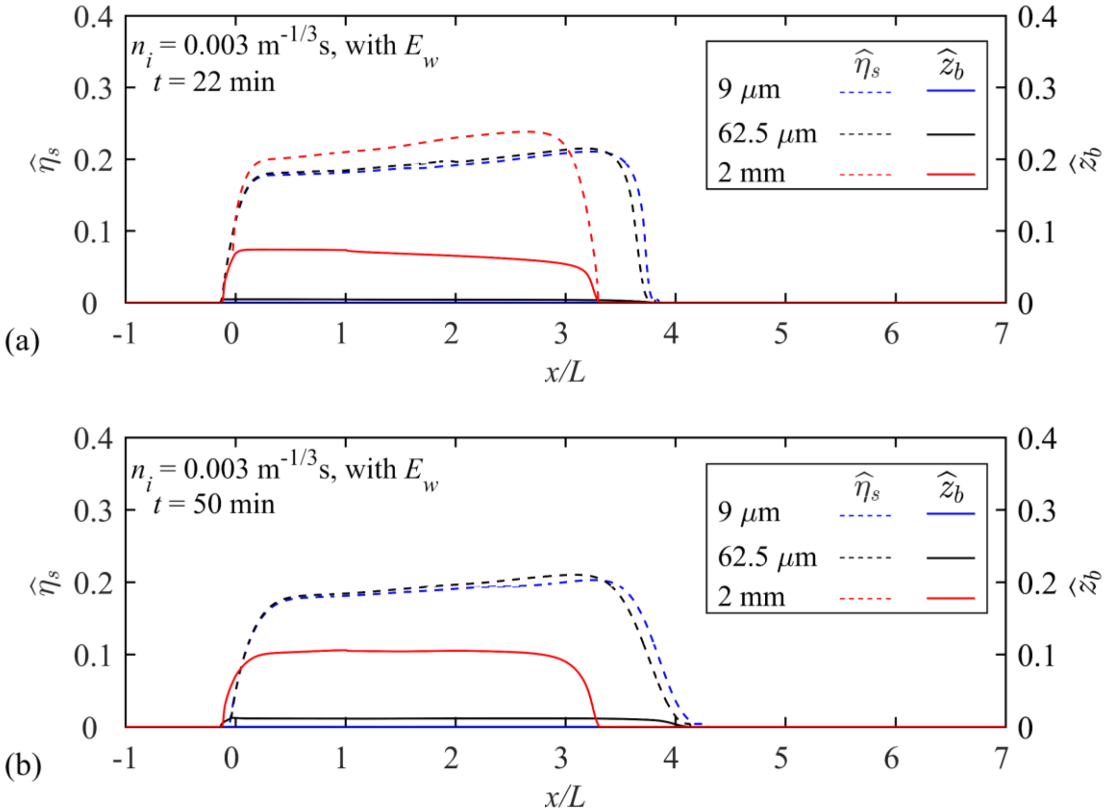

Fig. 4. Dimensionless free surface level $\hat{\eta}_s = h_s/h_{s0} + \hat{z}_b$ and dimensionless bed deformation $\hat{z}_b = (z_b - z_0)/h_{s0}$ spatial profiles of debris flow, predicted for three values of sediment particle diameter d at times (a) $t = 22$ min and (b) $t = 50$ min.

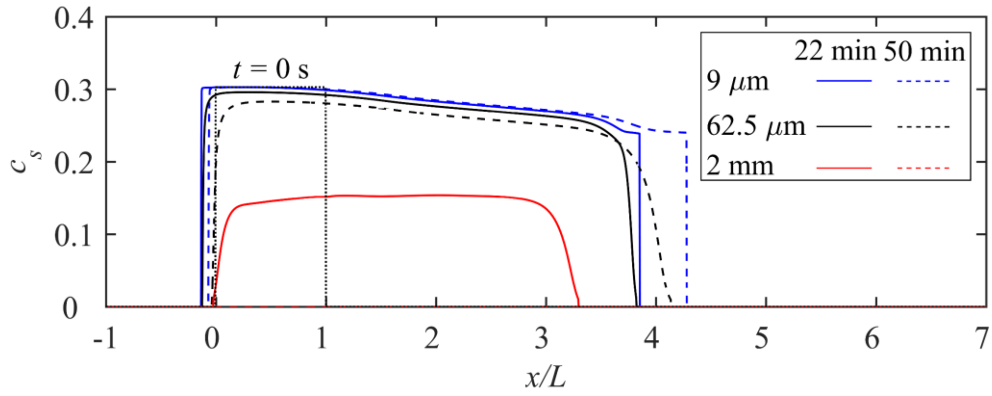

Fig. 5. Volumetric sediment concentration c_s spatial profile of debris flow, for three values of sediment particle diameter d at times t = 22 min and 50 min.

3.2. Laboratory-scale turbidity current

As a subaerial sediment-laden flow enters a reservoir it may plunge under overlying water to form a subaqueous sediment-laden flow called a turbidity current. In theory, a relatively highly concentrated turbidity current may exhibit non-Newtonian behavior, unlike a dilute turbidity current which exhibits almost Newtonian behavior. The second set of validation tests relate to a series of physical experiments on tributary turbidity currents conducted by Wang et al. (2020) using a glass flume, which contained a main channel (0.45 m wide, 30 m long, and bed slope $i_{bm} = 0.015$) and a tributary (0.3 m wide, 10 m long, and bed slope $i_{bt} = 0.005$) joined at 90° to the main channel a distance of 20 m from the outlet of main channel, as shown in Fig. S6 in the Supporting Information online.

Table 1. Selected cases for reservoir turbidity currents (E from Wang et al. 2020, and D hypothetical).

Series	Case	Q_t (L/s)	C_t $\left(\mathrm{kg/m^3}\right)$	h_{si} (m)
E	E1	1.98	300	0.17
	E2	4	300	0.21
D	D1	4	600	0.21

Table 1 lists key flow parameters for two experimental cases, E1 and E2 (taken from Wang et al., 2020), and one hypothetical case, D1, the last case corresponding to a relatively highly concentrated sediment-laden tributary inflow. As in the experiments, the numerical flume is initially full of still clear water with the water depth set at 0.45 m at the reservoir-tributary confluence. At the tributary inlet, the prescribed discharge Q_t, thickness h_{si} and sediment concentration C_t (Table 1) of the lower sediment-laden flow layer are kept constant, with no clear-water inflow. At the inlet of the main channel, there is no inflow. At the outlet, a constant free surface level is maintained using a tailgate. At the outlet, a free outflow boundary condition is imposed on the lower sediment-laden flow layer, the thickness of the clear-water flow layer is calculated according to a prescribed free surface level, and the layer velocity determined by the method of characteristics. The sediment has properties of suspended material taken from the Yellow River, China, with specific gravity of 2.65 and mean particle diameter of 7 μm. The interface roughness Manning coefficient is set as $n_i = 0.005\,\mathrm{m^{-1/3}}$, following Cao et al. (2015). The numerical grid spatial increments Δx and Δy are set to 0.025 m.

3.2.1. Validation against physical experiments

Fig. S7 in the Supporting Information and Fig. 6 display the measured and computed interface elevation η_s profiles along the central axes of the main channel and tributary for cases E1 and E2 with different inflow discharges. The range of interface elevation η_s was recorded at two instants, once when the front of the tributary turbidity current arrived at each cross-section and once when it reached a stable state. Because sediment concentrations of tributary inflow in cases E1 and E2 are close to the threshold concentration c_{vo} transformed from the Newtonian fluid to non-Newtonian fluid, computational results of two models, i.e., EDL model and ODL model, are compared against measured data. Model calibration is conducted with computational results of case E1 (see Fig. S7 in the Supporting Information), through which the Manning coefficient $n_b = 0.015\,\mathrm{m}^{-1/3}\mathrm{s}$ for both the EDL model and ODL model, and the coefficient $\phi = 0.85$ for EDL are adopted. Using the calibrated coefficients, the computational results for Case E2 with a larger discharge Q_t agree well with the measured data of the interface elevation η_s, as confirmed by the coefficients of determination $R^2{}_{\mathrm{ODL}}$ = 0.982 and $R^2{}_{\mathrm{EDL}}$ = 0.981 (Fig. 6a). Comparatively, because the sediment concentration of tributary inflow in Case E2 is slightly higher than the threshold concentration c_{vo}, there are marginal differences in interface elevation η_s between the ODL model and EDL model, and the final runout distance in UMC (upstream reach of the main channel) of the turbidity current predicted by the EDL model is slightly shorter than that by the ODL model (Figs. 6b and 6c). These results confirm the EDL model is applicable to dilute turbidity currents, which may be assumed Newtonian.

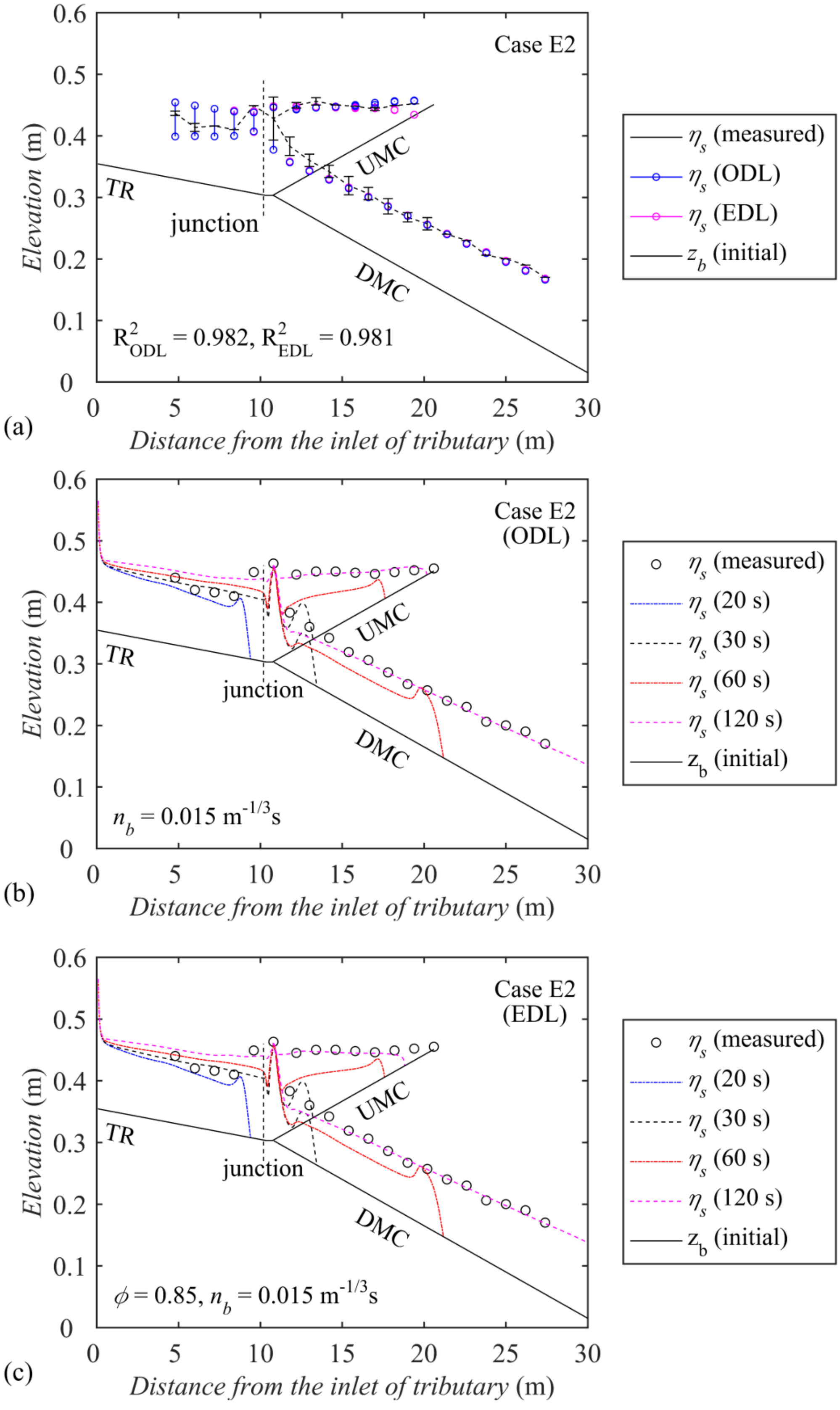

Fig. 6. Case E2 with tributary discharge $Q_t = 4\ \mathrm{L/s}$. (a) Comparison between measured and

computed ranges of interface elevation η_s at each cross-section. (b) ODL model and (c) EDL model predictions, and experimental measurements (Wang et al., 2020) of front elevation and interface elevation profiles along the central axes of the main channel (MC) and tributary (TR) at four time instants. Abbreviations UMC and DMC refer to upstream and downstream reaches of the main channel.

3.2.2. Designed cases

Turbidity currents with high sediment concentration differ substantially from those with dilute sediment concentration. Therefore, unlike experimental cases E1 and E2 involving dilute turbidity currents that are almost Newtonian, the hypothetical case D1 is designed to simulate a turbidity current of relatively high sediment concentration, which exhibits non-Newtonian behavior. This hypothetical case enables basic understanding of hyperconcentrated turbidity currents to be obtained, which should translate to large-scale simulations of hyperconcentrated turbidity currents in natural rivers.

3.2.2.1. Impact of non-Newtonian rheology on turbidity current propagation

Fig. 7 displays the evolution of interface elevation η_s in the main channel and tributary for Case D1 computed using the EDL and ODL models. After sustained, sediment-laden inflow from the bottom of the tributary inlet, a turbidity current forms as the turbidity volume slumps into clear water because of the driving force arising from the density difference. Upon arrival of the turbidity current front at the junction (Figs. 7a and 7b), the front elevation rises rapidly and the current propagates simultaneously upstream and downstream along the main channel. The turbidity current front thickness in the DMC (downstream reach of the main channel) increases longitudinally because of water entrainment, while that in the UMC decelerates gradually with time (Fig. 7c). By $t = 120\,\mathrm{s}$, the front of the turbidity current in DMC has been vented through the outlet, whilst the turbidity current front extended in UMC has stabilised (Fig. 7d).

In Fig 7, pronounced differences are evident in the results produced by the EDL and ODL models. Even though both models utilise the same initial and boundary conditions, the EDL model predicts slower turbidity current propagation in the DMC and smaller final runout distance of the turbidity front in the UMC than the ODL model. This is to be expected because the turbidity current computed using the ODL model is not controlled by yield stress, unlike the EDL model, and so facilitates a larger flow velocity and a longer runout distance.

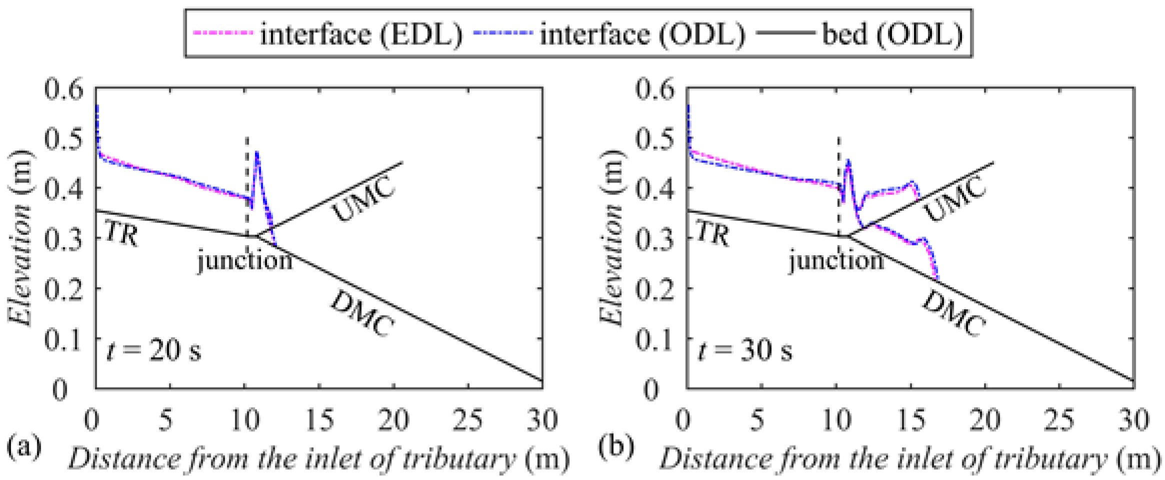

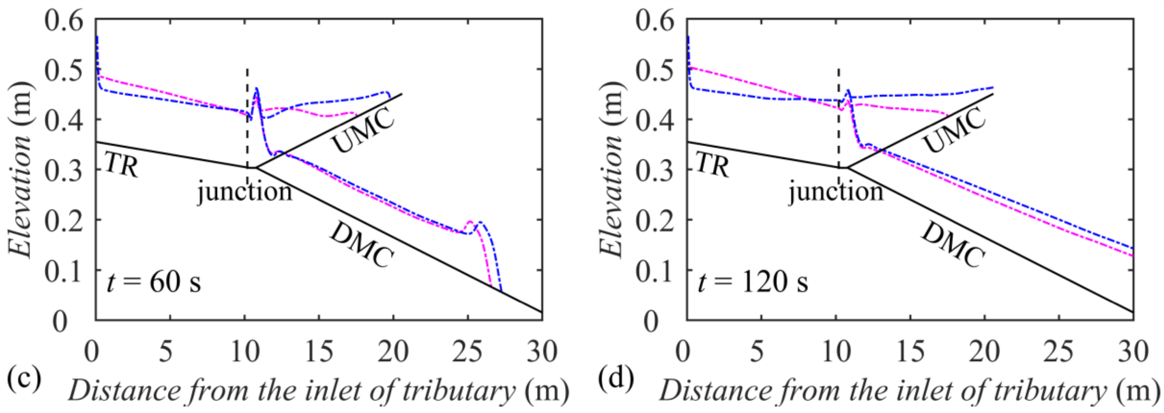

Fig. 7. Distribution of interface elevation η_s for Case D1 computed using ODL and EDL models at four time instants: (a) $t = 20\text{s}$, (b) $t = 30\text{s}$, (c) $t = 60\text{s}$, and (d) $t = 120\text{s}$. Abbreviations UMC and DMC refer to upstream and downstream reaches of the main channel.

3.2.2.2. Impact of non-Newtonian rheology on velocity field of turbidity current

We now examine the effect of non-Newtonian properties on the magnitude of layer-averaged velocity ($\overline{U_s} = \sqrt{U_s^2 + V_s^2}$) of the sediment-laden flow layer for Case D1 computed using the EDL model and reference (Newtonian) ODL model at times $t = 20$ s, 30 s, 60 s, and 120 s. In both simulations, by t = 30 s, the front of tributary turbidity current has reached the junction and intrudes into the main channel (propagating upstream and downstream simultaneously). The layer-averaged speed of the turbidity current decreases both as it propagates into the UMC and at the corner of the upstream junction where a small recirculation zone occurs. A second flow separation bubble and a region of maximum flow speed near the middle of the main channel develop immediately downstream of the junction as the turbidity current propagates into the DMC (Figs. 8a1 and 8a2). The speed of the sediment-laden layer in the UMC is lower than that in the DMC. Arguably, this is because interface shear stresses are larger when the turbidity current from the tributary propagates upstream along the main channel. At $t = 120$ s, the turbidity current speed decreases inside the tributary mouth as the current thickness increases. The turbidity current front extending along the UMC is stable and almost unchanging (Fig.7), and its speed falls asymptotically to zero because of energy dissipation. A zone of maximum speed is apparent in the main channel just downstream of the junction.

The EDL and ODL models exhibit similarity in terms of predicted flow structure, even though their estimates of bed shear stress differ. Apparent differences occur in the velocity fields predicted by the EDL and ODL models. The turbidity current predicted by the ODL model has a larger flow speed inside the tributary mouth than that by the EDL model. Moreover, the ODL model results contain a zone of maximum flow speed, which is likely a result of zero yield stress. Even though the ODL model produces a current of excessive flow speed that enlarges local viscous stresses, it nevertheless confirms the impact of yield stress on the modeling of turbidity currents.

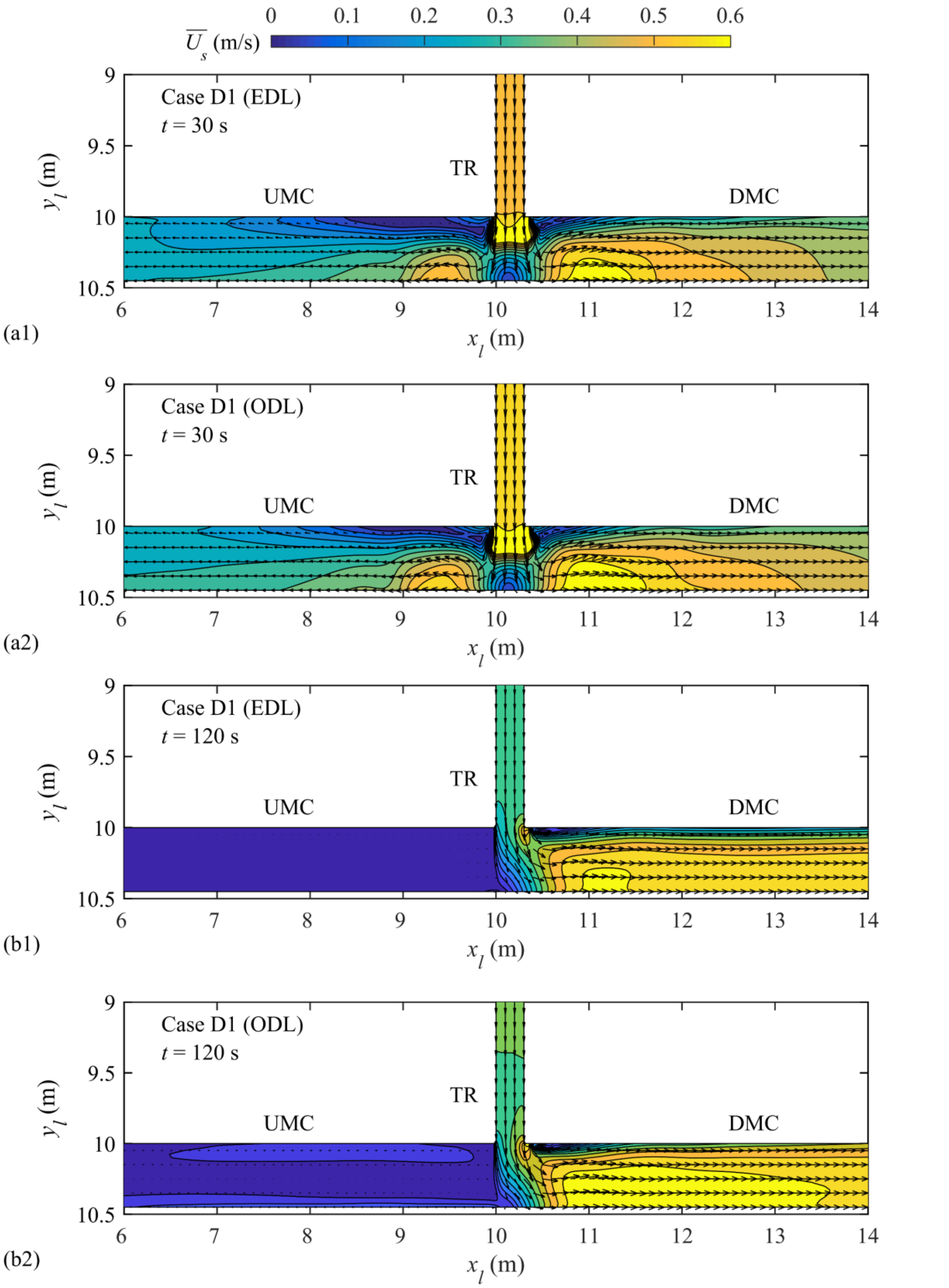

Fig. 8. Velocity fields for turbidity current Case D1 computed using (a1, b1) EDL model and (a2, b2) ODL model at times $t = 30\,\mathrm{s}$ and $t = 120\,\mathrm{s}$.

3.2.2.3. Impact of non-Newtonian rheology on sediment transport

Figs. 9 to 11 display the effects of non-Newtonian rheology on volumetric sediment concentration, and transverse and longitudinal sediment transport rates per unit channel width for Case D1. As the tributary turbidity current intrudes into the main channel, the sediment concentration in the main channel decreases longitudinally, and the lowest sediment concentration occurs at the intrusion front (Fig. 9). The transverse sediment transport rate per unit width $\mathrm{STR}_y \left(= h_s c_s V_s\right)$ of the turbidity current decreases as it propagates into the main channel (Fig. 10a). It exhibits almost no change inside the tributary from 30 s to 120 s owing to the imposed steady upstream boundary condition (Figs. 10b-10c). The longitudinal sediment transport rate per unit width $\mathrm{STR}_x \left(= h_s c_s U_s\right)$ of the turbidity current is negative in the UMC and asymptotically approaches zero after it is vented through the outlet, whereas it is positive in the DMC, increasing in the region of maximum speed but decreasing within the flow separation zone (Fig. 11).

During the first 20 s or so, the turbidity current front with low sediment concentration reaches the junction and differences between the EDL and ODL model predictions of STR_y and STR_x are slight (Figs. 10a and 11a). However, from 30 s to 120 s, even though high sediment concentration ($c_s > 0.16$) is more widely distributed in the EDL model than the ODL model predictions, the EDL model estimates of STR_y and STR_x are smaller than that of the ODL model inside the tributary mouth and within the maximum velocity zone. This is primarily because the EDL model rheology facilitates higher bed shear resistance than the ODL model, reducing the flow speed and, hence, the sediment transport rate.

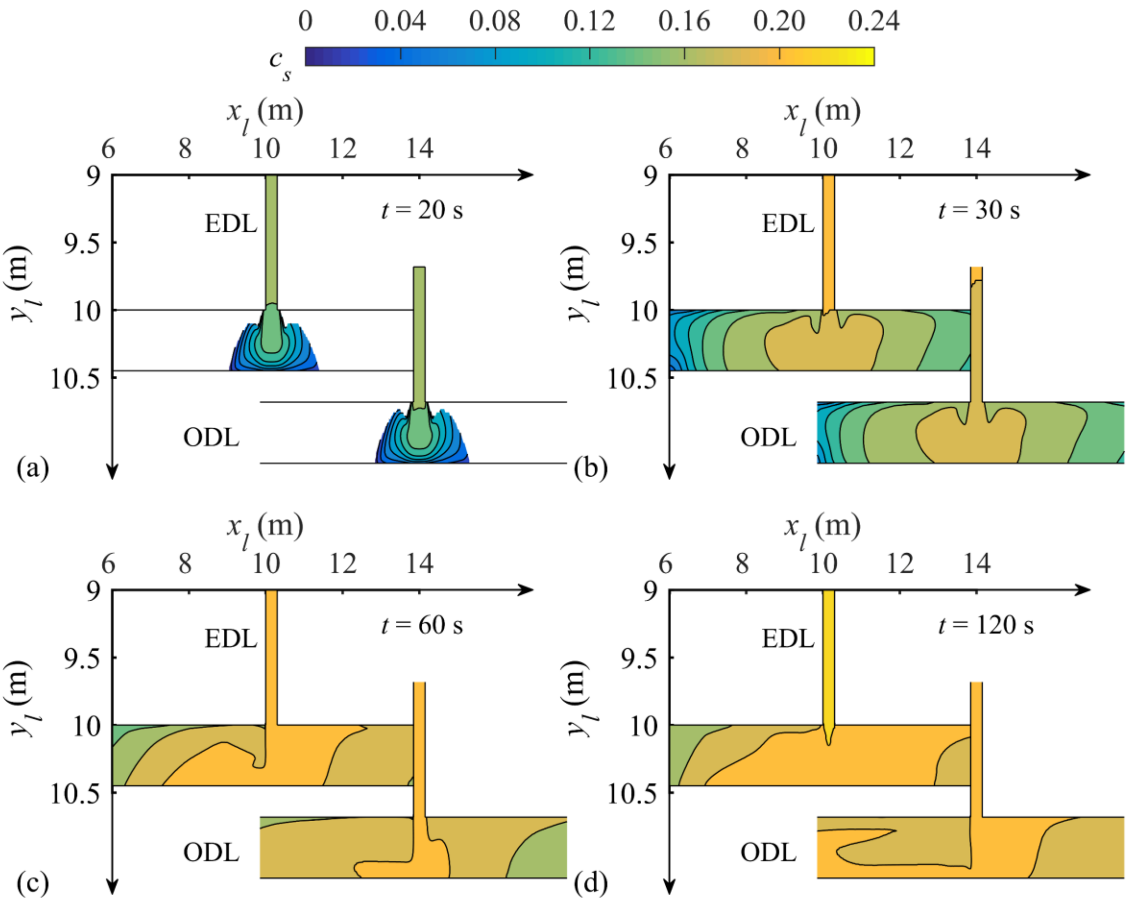

Fig. 9. Contour plots of sediment concentration c_s for turbidity current Case D1, computed using the ODL and EDL models at four time instants: (a) $t = 20\,\mathrm{s}$, (b) $t = 30\,\mathrm{s}$, (c) $t = 60\,\mathrm{s}$, and (d) $t = 120\,\mathrm{s}$.

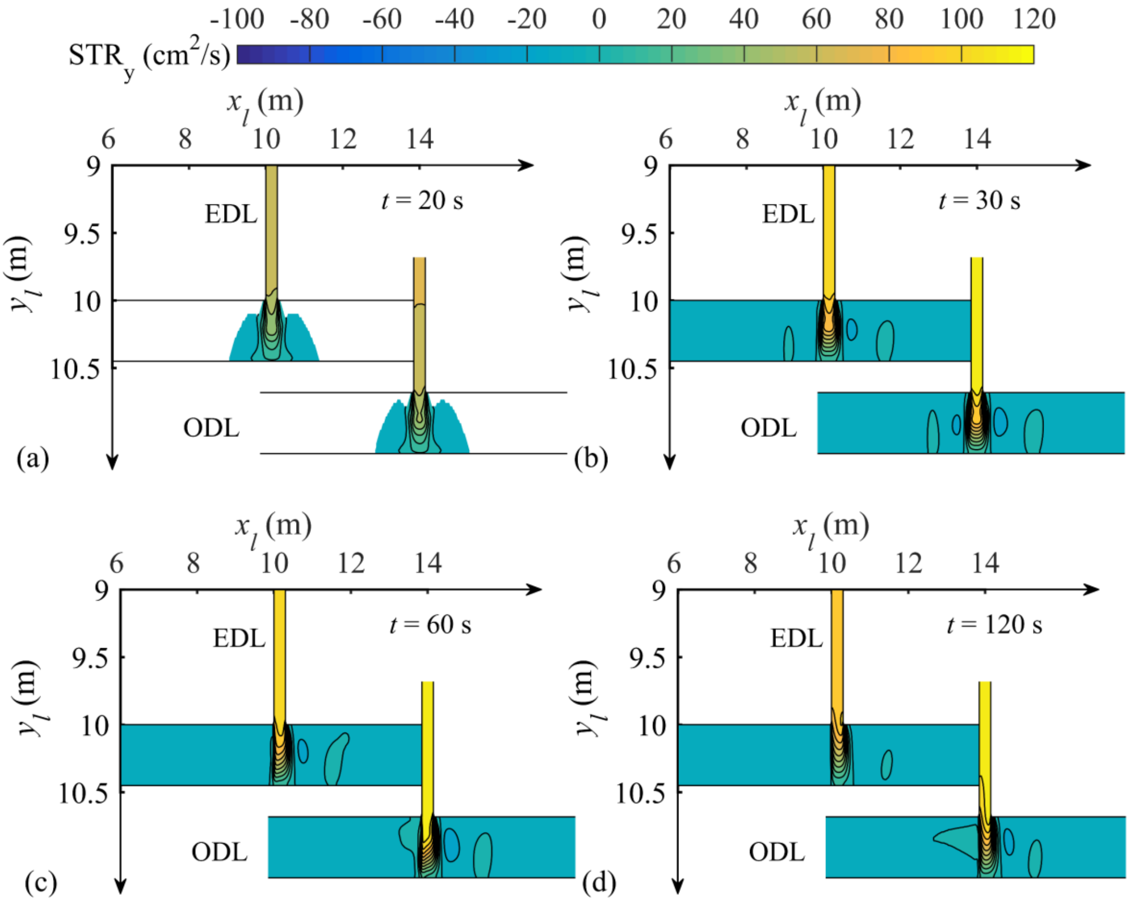

Fig. 10. Contour plots of transverse sediment transport rate per unit width $\mathrm{STR_y}$ near the confluence for Case D1, computed using the EDL and ODL models at four time instants: (a) $t = 20\,\mathrm{s}$, (b) $t = 30\,\mathrm{s}$, (c) $t = 60\,\mathrm{s}$, and (d) $t = 120\,\mathrm{s}$.

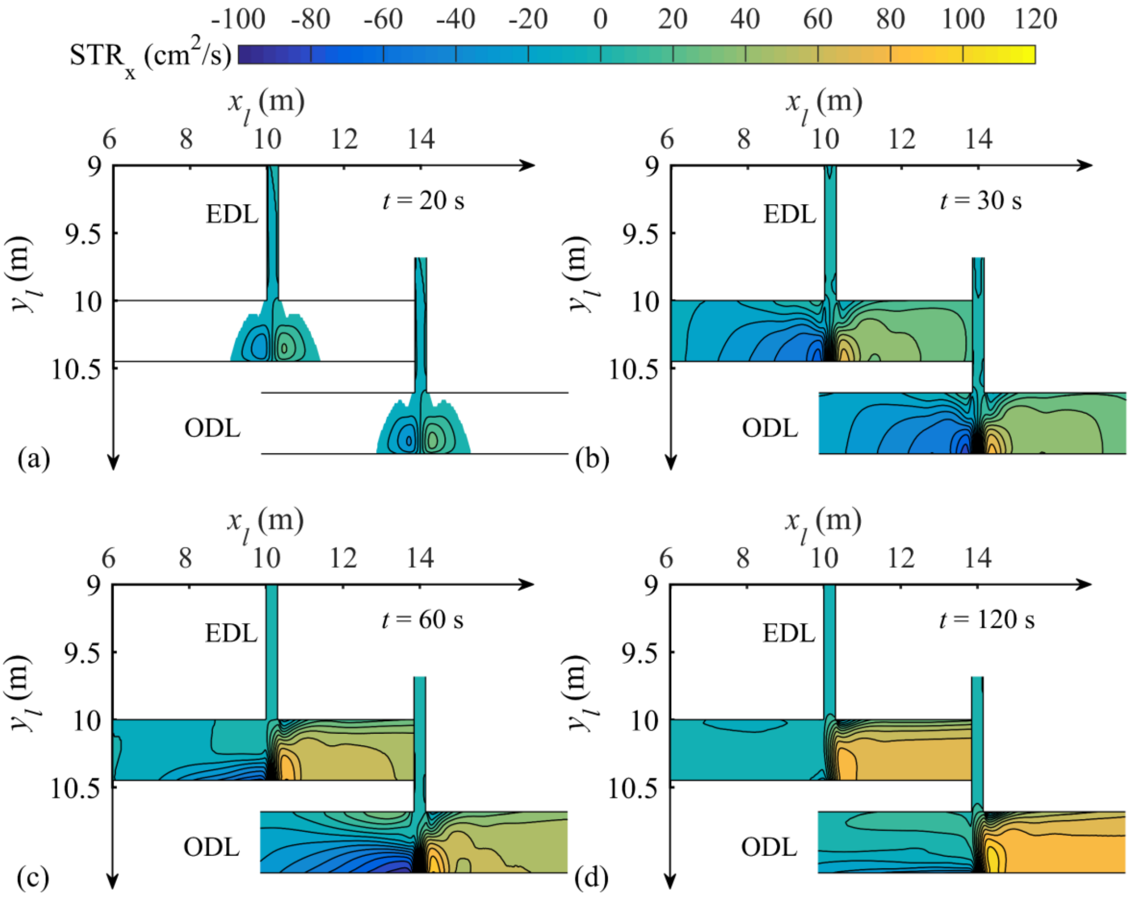

Fig. 11. Contour plots of longitudinal sediment transport rate per unit width STR_x near the confluence for Case D1 computed using the EDL and ODL models at four time instants: (a) $t = 20\,\mathrm{s}$, (b) $t = 30\,\mathrm{s}$, (c) $t = 60\,\mathrm{s}$, and (d) $t = 120\,\mathrm{s}$.

3.2.2.4. Impact of non-Newtonian rheology on bed shear stress

It is revealing to investigate differences in bed shear stress computed by the non-Newtonian EDL and Newtonian ODL models. Fig. 12 depicts the bed shear stress distribution for Case D1 at times $t = 20\,\mathrm{s}, 30\,\mathrm{s}, 60\,\mathrm{s}$, and 120 s. By t = 30 s, the tributary turbidity current has reached the junction and intruded into the main channel, and the volumetric sediment concentration near the confluence is approximately equivalent to the threshold concentration of a Bingham fluid c_{vo} (Figs.9a and 9b). At the junction, the bed shear stress with non-Newtonian characteristics is similar to that with Newtonian rheology, with the maximum velocity zone experiencing a high level of bed shear stress (Figs. 12a and 12b). Moreover, the volumetric sediment concentration inside the tributary by the EDL model is higher than that by the ODL model (Fig. 9b). Here, the bed shear stress obtained using non-Newtonian rheology is larger than that using Newtonian rheology because of the presence of yield stress. (Fig. 12b). Later, between t = 60 s and 120 s (Figs. 12c and 12d), the bed shear stress predicted by the ODL model is generally below 1 N/m^2 in the UMC, but reaches about 3.5 N/m^2 in the region of maximum flow speed. The bed shear stress predicted by the EDL model is quite different in that it reaches approximately 2.5 N/m^2 in the UMC, and about 3 N/m^2 in the zone of maximum flow speed. This implies that the bed shear stress magnitude predicted by the EDL model is directly related to the sediment concentration distribution when higher than c_{vm}. Conversely, the bed shear stress magnitude predicted by the ODL model is only related to the velocity field of the turbidity current.

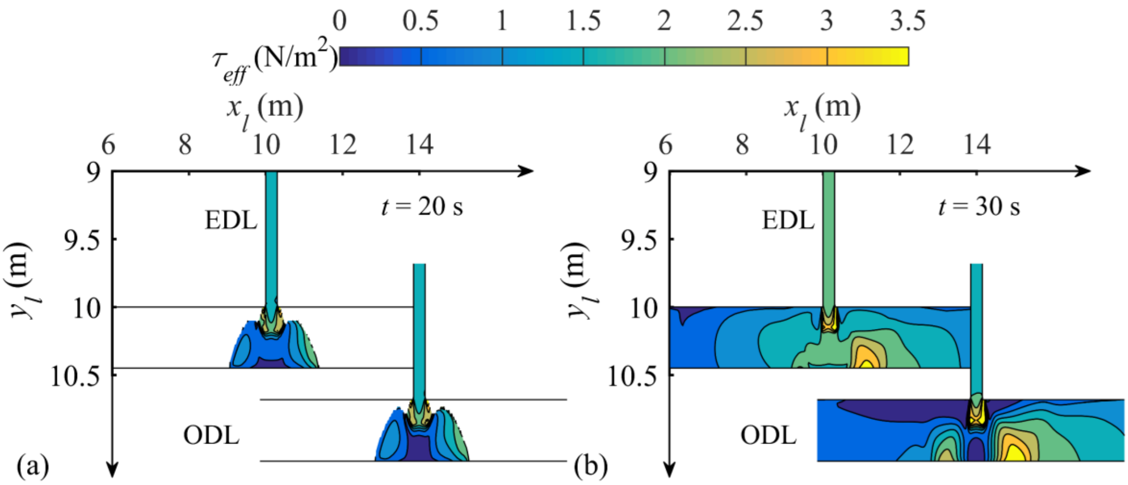

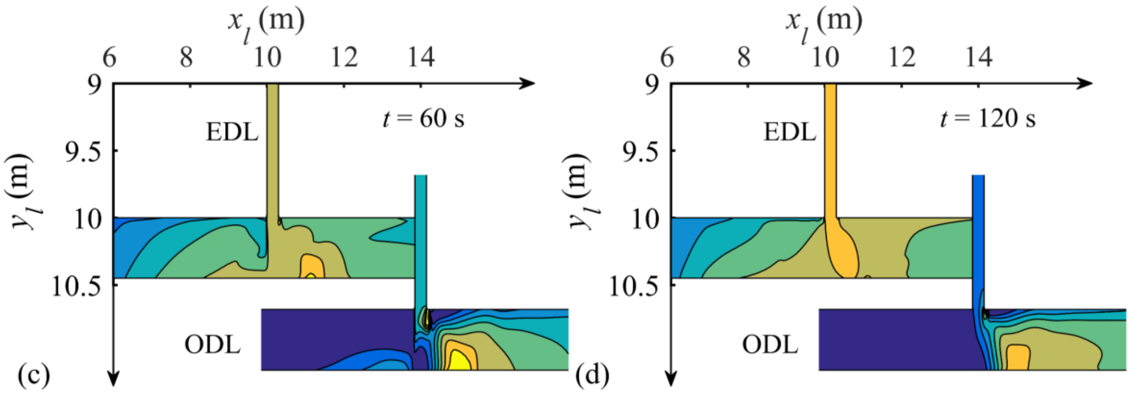

Fig. 12. Contours of bed shear stress τ_{eff} for Case D1 computed using EDL and ODL models at four time instants: (a) $t = 20\,\mathrm{s}$, (b) $t = 30\,\mathrm{s}$, (c) , $t = 60\,\mathrm{s}$ and (d) $t = 120\,\mathrm{s}$.

4. Model application – Guxian Reservoir, Yellow River

4.1. Study area

The Guxian Reservoir, planned for the middle Yellow River, China (Fig. 13), is likely to have tributary sediment inputs that account for more than 40% of the total sediment input (whose concentration could exceed 0.3) during extreme flood events and behave as a non-Newtonian fluid. We therefore select the Guxian Reservoir for a prototype-scale study. In our computational model, the initial bed topography is estimated from observed data acquired during April 2017. The domain comprises the main channel of the Yellow River from Wubu to the Guxian dam (approximately 200 km long and 300–1500 m wide), and a major tributary, Wuding River, from Baijiachuan to its junction with the main Yellow River. The study reach of the Wuding River is about 17 km long from the junction to Baijiachuan, located about 130 km upstream of the Guxian dam. Accurate topographic and hydrological data are unavailable for the other five tributaries with smaller discharges and lower sediment concentrations, and so these are neglected herein.

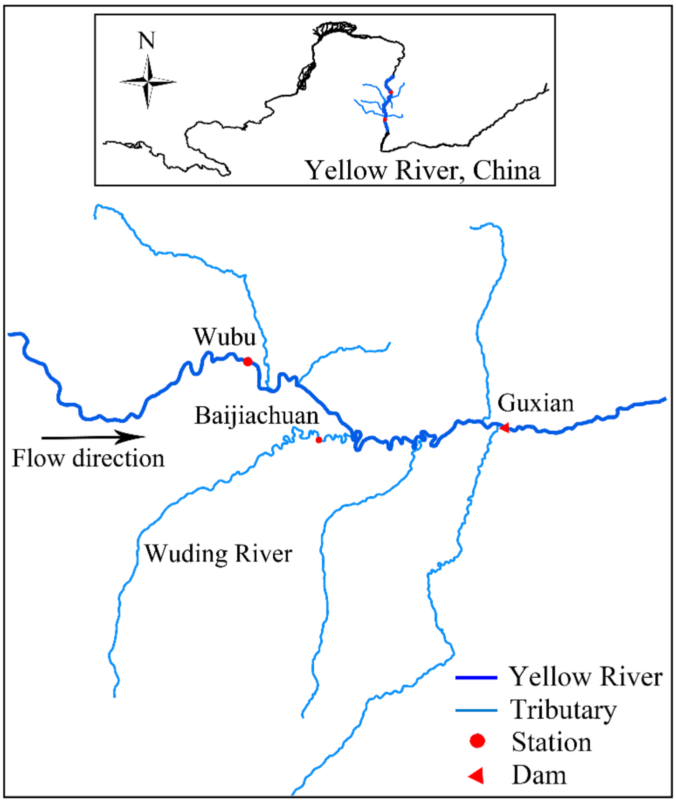

Fig. 13. Location of Guxian Reservoir and local tributaries along the Yellow River.

4.2. Model setup

Under normal operating conditions, the planned water level in the Guxian Reservoir is 627 m under the 1985 National Height Datum, China, corresponding to a total water storage capacity of 12.94×10^9 m^3. A fixed-bed, steady flow simulation is first conducted for gradually varied, clear-water inflow discharges specified at Wubu and Baijiachuan, and the resulting flow hydrodynamics taken as the initial condition for the present ODL and EDL models. Table 2 lists the flow discharge and sediment concentration input values at the two upstream boundary cross-sections (i.e., Wubu and Baijiachuan stations, Fig. 14). Noting the availability of observed data for input to the model, we simulate the evolution of turbidity currents for two highly concentrated sediment-laden floods that entered the Guxian Reservoir in July 2017 (Table 2, Wubu, and Fig. 14, Baijiachuan station). At the downstream boundary (Guxian dam), a boundary condition is not required for the turbidity current before its front arrives. The depth and velocity of the clear-water flow layer are determined by the method of characteristics according to the outflow discharge Q_{out}, which is kept constant at 6067 m^3/s, the design discharge for Guxian Reservoir.

Table 2. Inflow conditions for two prototype cases - Guxian Reservoir.

Wubu Station, Yellow River		Baijiachuan Station, Wuding River	
Q_{mi} (m^3/s)	C_{mi}	Q_{ti} (m^3/s)	C_{ti}
3600	0.069	Time series for July 2017 flood, Fig. 14	

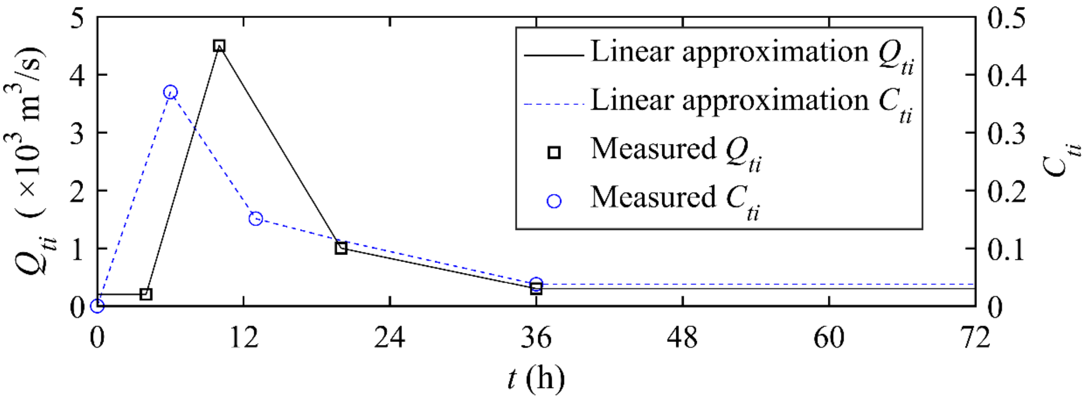

Fig. 14. Guxian reservoir study: observed data and piece-wise linear approximations of flow discharge hydrograph and sediment concentration time series at Baijiachuan station for a super-concentrated flood lasting from 0:00 a.m. July 26 to 0:00 a.m. July 29, 2017.

The following parameters are specified based on data from the middle Yellow River: mean sediment particle size $d = 25\ \mu\text{m}$, bed sediment porosity $p = 0.4$, and sediment density $\rho_s = 2650\ \text{kg/m}^3$. The computational grid is uniform with 35 m spacing in both longitudinal and lateral directions. The Courant number is set to 0.4. In the ODL model, the bed roughness Manning coefficient n_b is set to $0.03\,\mathrm{m^{-1/3}s}$; in the EDL model the yield stress and dynamic viscosity are estimated using Eqs. (17) and (18) with $\phi = 0.7$. In both models, the interface roughness Manning coefficient n_i is set to $0.005\,\mathrm{m^{-1/3}s}$, following Cao et al. (2015).

4.3. Results and discussion

Here we examine the influence of the rheological characteristics on the formation and propagation of reservoir turbidity currents and bed deformation in the Guxian Reservoir domain based on simulations using the EDL model and ODL model.

In general, the transition from subaerial open channel sediment-laden flow to subaqueous turbid flow features the formation of a reservoir turbidity current with unstable plunge points that propagate forward. Figs. 15b1 and 15b2 show that by t = 12 h, the subaerial sediment-laden flows in the MC (main channel) and WR (Wuding River) have plunged into clear water and formed turbidity currents, whilst the front of the WR turbidity current has intruded into the MC and propagated both upstream and downstream simultaneously. By t = 24 h, the front of the WR turbidity current has mixed with the MC turbidity current and is propagating downstream with high interface elevation at the junction (Figs. 15c1 and 15c2). At t = 48 h, as the sediment input from WR decreases, the thickness of the turbidity current increases in WR (Figs. 15d1 and 15d2). This primarily occurs because Ri reduces progressively with lowering sediment concentration, and thus induces greater water entrainment E_w. At t = 72 h, the plunge point is located downstream of the junction in the MC, and the upper clear-water layer in the WR disappears (Figs. 15e1 and 15e2). Moreover, as it is slowing, the MC turbidity current has not yet arrived at the Guxian dam. This is because the sediment input from the WR decreases, and sedimentation occurs within WR and near the river confluence (Fig. 16), which correspondingly reduces both the density and the driving force of the turbidity currents.

The EDL and ODL model results display pronounced differences in the hydro-sediment-morphological processes associated with hyperconcentrated turbidity currents. When the sediment concentration of the turbidity current exceeds the threshold concentration c_{vo} of non-Newtonian fluid, the bed boundary resistance computed using the EDL model is larger than that using the ODL model (Figs. 17a1 and 17a2). Hence, the propagation of turbidity current predicted by the EDL model is slower than that by the ODL model (Figs. 15b1 and 15b2, Fig. S8 in the Supporting Information). However, after $t \sim 12$ h, the sediment concentration of the reservoir turbidity current falls below the threshold concentration c_{vo} (Fig. S9 in the Supporting Information). This means that the turbidity current gradually dilutes and its behaviour approaches that of a Newtonian flow. Notably, the EDL model predicts larger bed aggradation at the confluence than the ODL model (Figs. 16a and 16b). In response to the greater boundary resistance, the decreasing velocity of the turbidity current lowers the sediment entrainment flux, leading to reduced sediment concentration and a smaller driving force for the turbidity current. Therefore, the hyperconcentrated turbidity current predicted by the EDL model features slower propagation and more significant sedimentation than that by the ODL model.

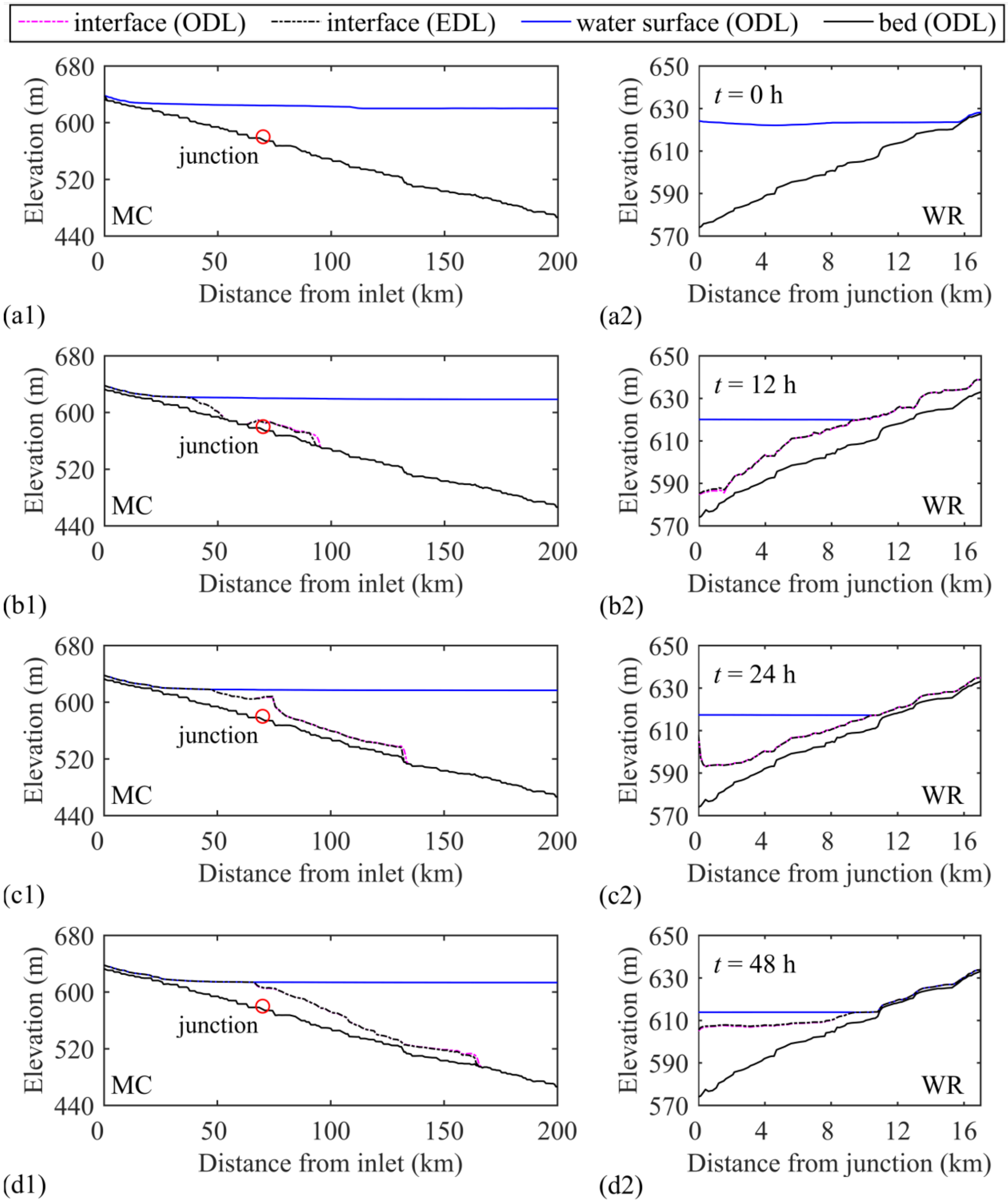

Fig. 15. Guxian reservoir study: water surface, interface and bed profiles along the thalweg of (a1-e1) main channel (MC) and (a2-e2) Wuding River (WR) computed using the ODL and EDL models at time instants, t = 0 h, 12 h, 24 h, 48 h and 72 h.

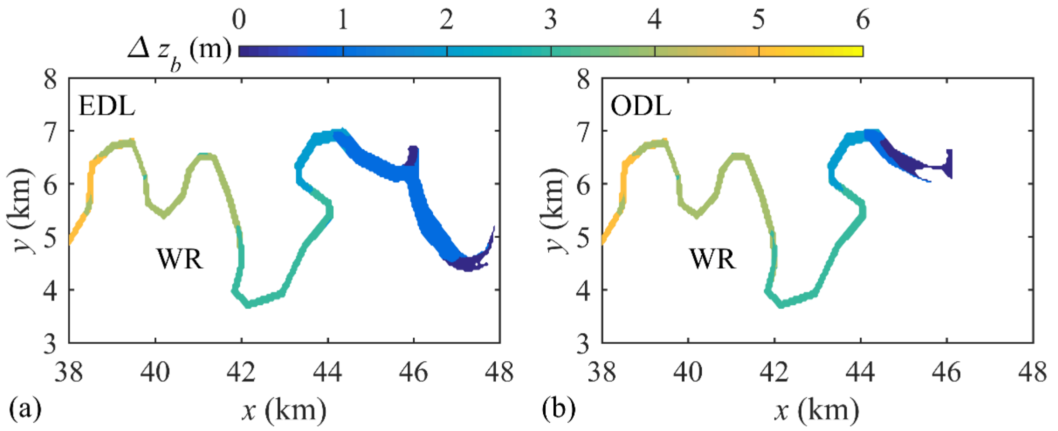

Fig. 16. Guxian reservoir study: contours of bed deformation depth $\Delta z_b = z_b(x, y, t) - z_b(x, y, 0)$ at time $t = 72\,\text{h}$ predicted by (a) EDL model and (b) ODL model.

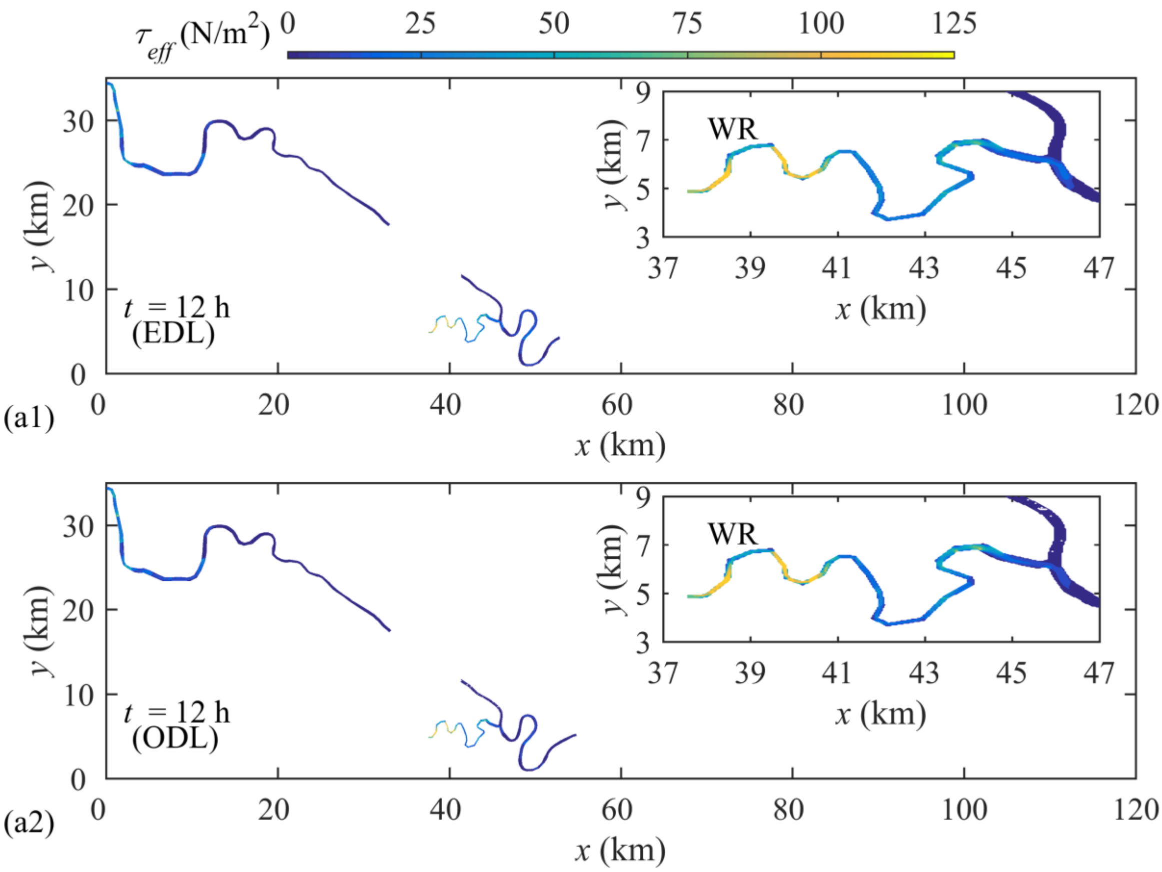

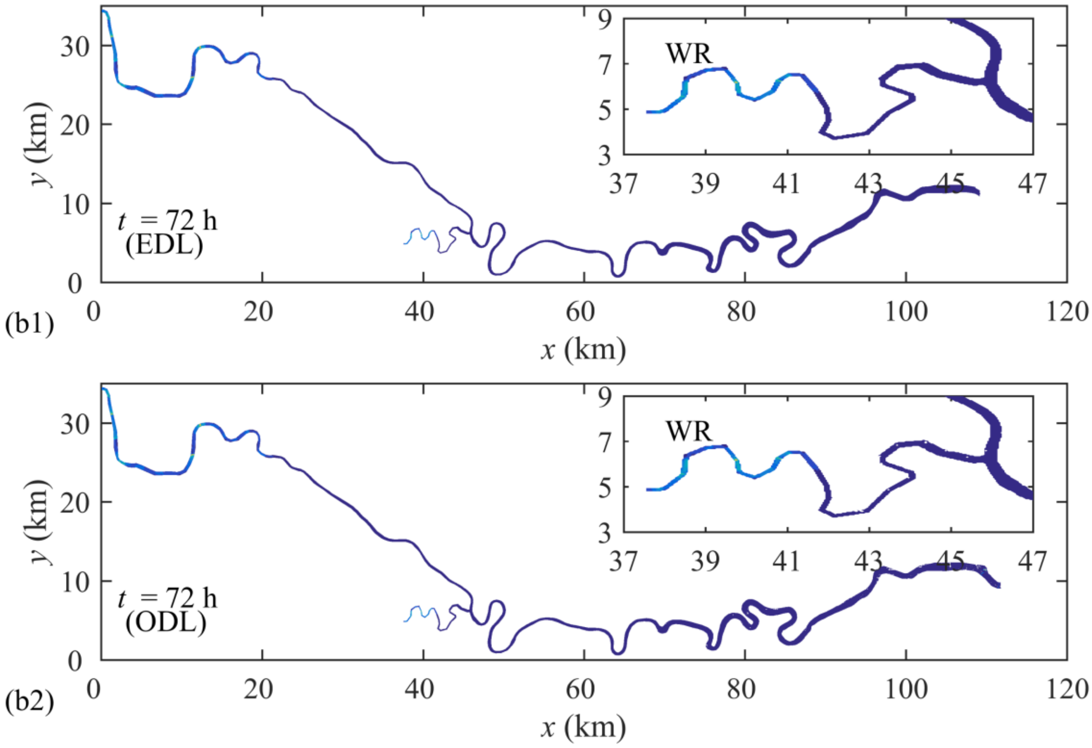

Fig. 17. Guxian reservoir study: distributions of bed shear stress τ_{eff} at time instants t = 12 h and 72 h, predicted using (a1-b1) EDL model and (a2-b2) ODL model.

5. Conclusions

A two-dimensional double layer-averaged model has been proposed that incorporates non-Newtonian constitutive properties of yield stress and shear-thinning, and resolves the holistic physical processes behind the formation and propagation of turbidity currents. Both Newtonian (ODL) and non-Newtonian (EDL) models were applied to resolve hyperconcentrated subaerial mud flows, subaqueous debris flows, and reservoir turbidity currents. For hyperconcentrated turbidity currents, it was found that as the yield stress τ_Y decreases to zero, the non-Newtonian flow transforms into a Newtonian flow. The power coefficient n, which represents shear-thinning or shear-thickening phenomena, plays a key role in the large range of shearing rates encountered in non-Newtonian flows, with increasing power coefficient n leading to larger turbidy current thickness and slower propagation. Interface interactions between the subaqueous non-Newtonian flow underlayer and ambient water overlayer play a critical part in the evolution of the turbidity current. Water entrainment causes both the front thickness and final runout distance of a non-Newtonian turbidity current to increase, whereas interfacial resistance has a secondary effect. Hardly any sedimentation occurs in a non-Newtonian flow carrying fine particles, as would be expected.

The present EDL model and ODL model predict very similar behaviour for dilute concentrated turbidity currents, confirming that the EDL model is effectively the same as an ODL model in cases where non-Newtonian behavior is negligible. When sediment concentration exceeds a threshold value, pronounced differences develop between the predictions by the EDL and ODL models of the evolution of a hyperconcentrated turbidity current. Unlike the Newtonian model, the EDL model predicts slower propagation of the turbidity current and more significant bed aggradation, causing a feedback effect on the evolution of the turbidity current through decreased turbidity current density and reduced driving force.

The present findings demonstrate that it is essential to account for non-Newtonian rheology when modelling a hyperconcentrated turbidity current. This has significant implications for the simulation of hydro-sediment-morphological processes, and hence the sediment management of reservoirs in sandy river basins. Moreover, in a turbidity current with uniform sediment, the particle diameter has an inherent impact on bed deformation. Further laboratory and field investigations are needed to study bed deformation induced by hyperconcentrated sediment-laden flows carrying non-uniform sediment.

Acknowledgments

This work has been funded by the National Natural Science Foundation of China under Grant No. 12072244.

References

Adebiyi, A. A. and Hu, P. (2021). A numerical study on impacts of sediment erosion/deposition on debris flow propagation. *Water*, *13*, 1968.

Balmforth, N. J. and Provenzale, A. (2010). *Geomorphological Fluid Mechanics*. Berlin, Springer.

Brufau, P., García-Navarro, P., Ghilardi, P. and Natale, L., et al. (2000). 1D Mathematical modelling of debris flow. *Journal of Hydraulic Research*, *38*(6), 435-446.

Cao, Z. X., Li, J., Pender, G. and Liu, Q. Q. (2015). Whole-process modeling of reservoir turbidity currents by a double layer-averaged model. *Journal of Hydraulic Engineering*, *141*(2), 04014069.

Cao, Z. X., Pender, G. and Carling, P. (2006). Shallow water hydrodynamic models for hyperconcentrated sediment-laden floods over erodible bed. *Advances in Water Resources*, *29*(4), 546-557.

Denlinger, R. P. and Iverson, R. M. (2001). Flow of variably fluidized granular masses across three-dimensional terrain 2. Numerical predictions and experimental tests. *Journal of Geophysical Research*, *106*(B1), 553-566.

Fedele, J. J. and García, M. H. (2009). Laboratory experiments on the formation of subaqueous depositional gullies by turbidity currents. *Marine Geology*, *258*(1), 48-59.

Fei, X. J. (1991). A model for calculating viscosity of sediment carrying flow in the middle and lower Yellow River. *Journal of Sediment Research*, *6*(2), 1-13. (in Chinese)

Georgoulas, A. N., Angelidis, P. B., Panagiotidis, T. G. and Kotsovinos, N. E. (2010). 3D numerical modelling of turbidity currents. *Environmental Fluid Mechanics*, *10*(6), 603-635.

Guo, Q. C., Hu, C. H., Takeuchi, K. and Ishidaira, H., et al. (2008). Numerical modeling of hyper-concentrated sediment transport in the lower Yellow River. *Journal of Hydraulic Research*, *46*(5), 659-667.

Hallworth, M. A. and Huppert, H. E. (1998). Abrupt transitions in high-concentration, particle-driven gravity currents. *Physics of Fluids*, *10*(5), 1083-1087.

Hou, J. M., Simons, F., Mahgoub, M. and Hinkelmann, R. (2013). A robust well-balanced model on unstructured grids for shallow water flows with wetting and drying over complex topography. *Computer Methods in Applied Mechanics and Engineering*, *257*, 126-149.

Hu, P. and Li, Y. (2020). Numerical modeling of the propagation and morphological changes of turbidity currents using a cost-saving strategy of solution updating. *International Journal of Sediment Research*, *35*(6), 587-599.

Huang, X. and Garcia, M. H. (1997). A perturbation solution for Bingham-plastic mudflows. *Journal of Hydraulic Engineering*, *123*(11), 986-994.

Imran, J., Parker, G., Locat, J. and Lee, H. (2001). 1D numerical model of muddy subaqueous and subaerial debris flows. *Journal of Hydraulic Engineering*, *127*(11), 959-968.

Jacobson, M. R. and Testik, F. Y. (2013). On the concentration structure of high-concentration constant-volume fluid mud gravity currents. *Physics of Fluids*, *25*(1), 016602.

Johnson, C. G., Kokelaar, B. P., Iverson, R. M. and Logan, M., et al. (2012). Grain-size segregation and levee formation in geophysical mass flows. *Journal of Geophysical Research - Earth Surface*, *117*, F01032.

Lai, Y. G., Huang, J. and Wu, K. (2015). Reservoir turbidity current modeling with a two-dimensional layer-averaged model. *Journal of Hydraulic Engineering*, *141*(12), 04015029.

Lee, H. Y. and Yu, W. S. (1997). Experimental study of reservoir turbidity current. *Journal of Hydraulic Engineering*, *123*(6), 520-528.

Li, J., Cao, Z. X., Pender, G. and Liu, Q. Q. (2015). Hyperbolicity analysis of a double layer-averaged model for open-channel sediment-laden flows. *Scientia Sinica: Physica, Mechanica ＆ Astronomica*, *45*(10), 104705. (in Chinese)

Locat, J. (1997). Normalized rheological behaviour of fine muds and their flow properties in a pseudoplastic regime. Proc., 1st International Conference on Debris-Flow Hazard

Mitigation. Reston, 260-269.

O' Brien, J. S. and Julien, P. Y. (1988). Laboratory analysis of mudflow properties. *Journal of Hydraulic Engineering*, *114*(8), 877-887.

Parker, G., Fukushima, Y. and Pantin, H. M. (1986). Self-accelerating turbidity currents. *Journal of Fluid Mechanics*, *171*(3), 145-181.

Pierson, T. C. and Scott, K. M. (1985). Downstream dilution of a lahar: Transition from debris flow to hyperconcentrated streamflow. *Water Resources Research*, *21*(10), 1511-1524.

Qian, X. S., Xu, J. P., Das, H. S. and Wang, D. W., et al. (2020). Improved modeling of subaerial and subaqueous muddy debris flows. *Journal of Hydraulic Engineering*, *146*(7), 06020007.

Richardson, J. F. and Zaki, W. N. (1997). Sedimentation and fluidisation: Part 1. *Chemical Engineering Research & Design*, *32*, S82-S100.

Toro, E. F. (2001). *Shock-Capturing Methods for Free-Surface Shallow Flows*. Chichester, U.K., Wiley.

Wang, T., Wang, Y. J., Ma, H. B. and Li, T., et al. (2020). Experimental study on flow and sediment evolution characteristics in conjunction area after confluence of density current at reservoir tributary. *Yellow River*, *42*(5), 56-61. (in Chinese)

Wang, W., Chen, G., Han, Z. and Zhou, S., et al. (2016). 3D numerical simulation of debris-flow motion using SPH method incorporating non-Newtonian fluid behavior. *Natural Hazards*, *81*(3), 1981-1998.

Wang, Z. Y., Qi, P. and Melching, C. S. (2009). Fluvial hydraulics of hyperconcentrated floods in Chinese rivers. *Earth Surface Processes and Landforms*, *7*(34), 981-993.

Wang, Z. Y., Wu, B. S. and Wang, G. Q. (2007). Fluvial processes and morphological response in the Yellow and Weihe Rivers to closure and operation of Sanmenxia Dam. *Geomorphology*, *91*(1-2), 65-79.

Wang, Z., Xia, J., Li, T. and Deng, S., et al. (2016). An integrated model coupling open-channel flow, turbidity current and flow exchanges between main river and tributaries in Xiaolangdi Reservoir, China. *Journal of Hydrology*, *543*, 548-561.

Wang, Z., Xia, J., Zhang, J. and Li, T. (2018). Modeling turbidity currents in the Xiaolangdi Reservoir with the effect of flow exchanges with tributaries. *Advanced Engineering Sciences*, *50*(1), 85-93. (in Chinese)

Wright, L. D., Wiseman, W. J., Bornhold, B. D. and Prior, D. B., et al. (1988). Marine dispersal and deposition of Yellow River silts by gravity-driven underflows. *Nature*, *332*, 629-632.

Wright, V. G. (1987). *Laboratory and numerical study of mud and debris flow*. PhD Dissertation, University of California, Davis, USA.

Wright, V. G. and Krone R. B. (1987). Laboratory and numerical study of mud and debris flow, *Proceedings XXII IAHR Symposium*, Lausanne, Switzerland.

Xia, C. C. and Tian, H. Y. (2022). A quasi-single-phase model for debris flows incorporating non-Newtonian fluid behavior. *Water*, *14*, 1369.

Zhang, R. J. and Xie, J. H. (1993). *Sedimentation Research in China: Systematic Selections.*

Beijing, China, China Water & Power Press (in Chinese).